ADVANCED FUNCTIONAL MATERIALS
www.afm-journal.de

Mesoporous Carbon Thin Films with Large Mesopores as Model Material for Electrochemical Applications

*Lysander Q. Wagner, Joshua Schober, Pascal Dippell, Chantal Glatthaar, Smail Mekhilef, David Schäfer, Hannes Hergert, Marcus Rohnke, Matthias T. Elm, and Bernd M. Smarsly**

The synthesis of mesoporous carbon thin films is proposed on titanium plates with well-ordered 70 nm mesopores via soft templating of resol resins with poly(ethylene oxide)-*block*-poly(hexyl acrylate) copolymers. Surprisingly, regular carbonization in pure argon suffers from a metal substrate corrosion not yet observed in literature. This corrosion phenomenon is investigated by secondary ion mass spectrometry, electron microscopy, and X-ray diffraction, and it is identified that the introduction of carbon monoxide into the carbonization atmosphere as successful approach to suppress substrate corrosion without changing microstructure, composition, or pore structure of the non-graphitic carbon. The model electrodes, which consist of a 200–300 nm thick mesoporous carbon layer, the titanium substrate, and a 200 nm thick titanium carbide interphase, are tested for their suitability as electrocatalyst support: The electric transport through and along the thin film is investigated by impedance and Hall measurements and contrasted to similarly mesoporous IrO_2 thin films. Accessibility of the pore system and electrochemical stability under acidic water-splitting conditions are studied by SIMS and cyclovoltammetry, respectively. The mesoporous carbon thin films reveal a conductivity similar to IrO_2, high stability, and (tunable) accessibility, rendering them a promising model system for several applications like electrocatalysis and sodium-ion batteries.

1. Introduction

In the framework of energy transition, hydrogen might play a major role for temporary energy storage if so-called green energy (from wind or solar power plants) is converted to hydrogen in case of an oversupply. This hydrogen can be stored easily until the energy demand requires a reconversion of the chemical energy into electric energy.[1,2] In acidic water electrolysis, though, precious catalyst materials are needed, like iridium dioxide for the anodic oxygen evolution reaction (OER).[1] To save critical and expensive materials, a substitution by a non-critical yet conducting catalyst support is desired, on which the actual catalyst is deposited in small quantities (for instance, by atomic layer deposition).

Ordered mesoporous carbon seems to be a particularly promising model material as a catalyst support due to the large surface area,[3,4] a high mechanical and chemical durability,[5] and its abundance. Consequently, mesoporous carbon has been studied for several applications, even beyond water splitting. As summarized in **Figure 1**, such mesoporous carbon films can be used among others for pollutant removal (like heavy metal ions),[6] heterogeneous catalysis (e.g., olefin hydration),[7] gas storage (for instance, hydrogen storage for fuel cell vehicles),[8] electrocatalysis,[4] and electrode materials for capacitors[4,8] and sodium-ion batteries.[4]

While in the first three applications a metal substrate is not required (but from an industrial point of view desirable when considering stainless steel reactors), a conductive substrate is mandatory for the remaining three applications (as an electrocatalyst, capacitor, or battery material) to ensure an electric contact. For this reason, we present a specially designed synthesis of carbon thin films with well-ordered 70 nm mesopores optimized for a metal substrate. Please note that the large spherical pores in this study (partly) lie in the macropore regime according to the IUPAC definition of mesopores (2–50 nm). However, the term "mesopores" is still used herein to avoid confusion with very large pores (hundreds of nanometers) when talking of "macropores", and with hierarchical pore systems when talking of "meso-/macropores". The synthesis is not trivial due to possible substrate corrosion, which we identified as an unexpected obstacle and might have been overseen in previous studies. The majority

L. Q. Wagner, J. Schober, P. Dippell, C. Glatthaar, S. Mekhilef, D. Schäfer, M. Rohnke, B. M. Smarsly
Institute of Physical Chemistry
Justus Liebig University
35392 Giessen, Germany
E-mail: bernd.smarsly@phys.chemie.uni-giessen.de

L. Q. Wagner, P. Dippell, C. Glatthaar, D. Schäfer, H. Hergert, M. Rohnke, M. T. Elm, B. M. Smarsly
Center of Materials Research
Justus Liebig University
35392 Giessen, Germany

H. Hergert, M. T. Elm
Institute of Experimental Physics I
Justus Liebig University
35392 Giessen, Germany

The ORCID identification number(s) for the author(s) of this article can be found under https://doi.org/10.1002/adfm.202521031

DOI: 10.1002/adfm.202521031

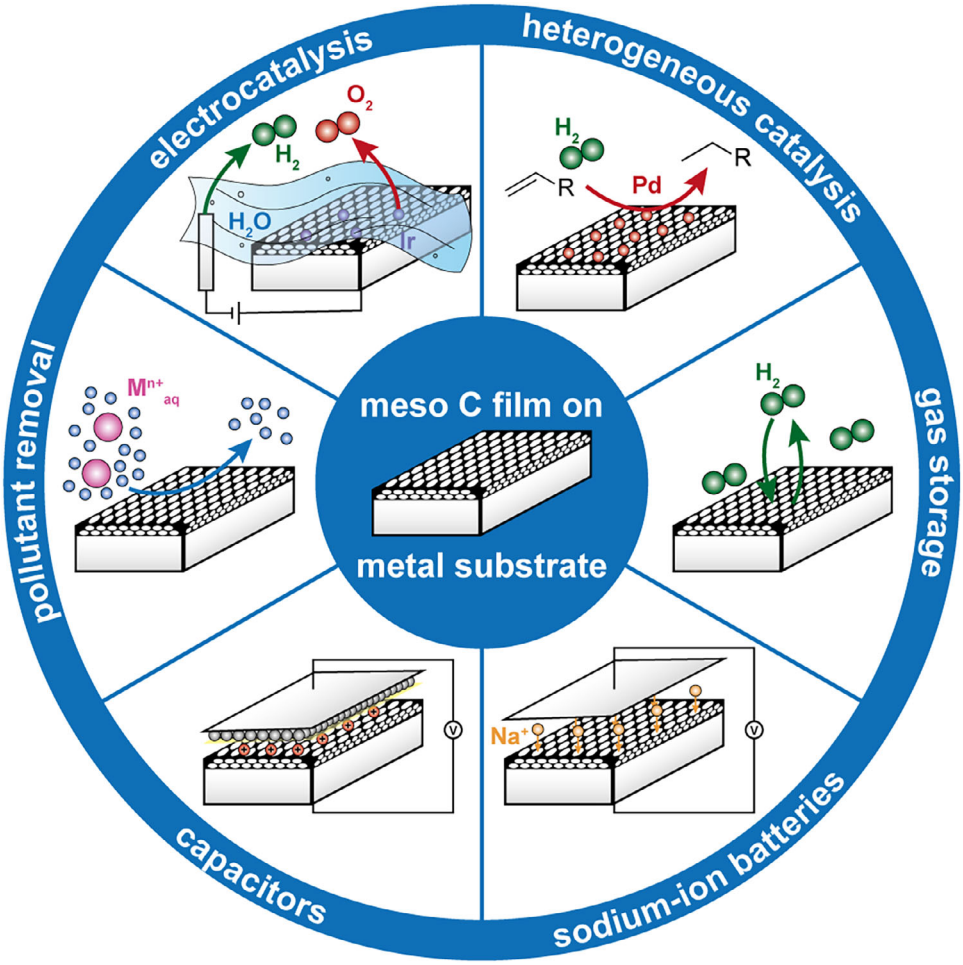

Figure 1. Possible applications of mesoporous carbon thin films deposited on metal substrates.

of articles on resin-derived carbon thin films base on samples prepared on silicon wafers, quartz glass, glassy carbon, and poly(ethylene terephthalate),[9–27] in which no alterations of the substrate were observed. Even works about carbon deposited on metal substrates such as stainless steel[7] and copper[28] do not report such a corrosion, which either might not have occurred there or remained undiscovered underneath the thick carbon film of 400–700 nm in size.

The template-based preparation of porous carbon materials seems to be well established, but there are still challenges in the synthesis, which are related to the transition from organic precursors (here: phenolic resins) to an amorphous and finally crystalline ("graphitic") carbon. It was particularly Helmut Cölfen who–as a pioneer–proposed and finally proved the groundbreaking idea that even highly ionic crystalline solids, such as $CaCO_3$,[29] may form through an amorphous particle, emphasizing the relevance of such pre-nucleation clusters[30–33] for the final material in nature. Interestingly, this concept holds true for the carbonization of organic materials, as some hydrocarbon-based materials, upon high-temperature treatment up to 3000 °C, form graphite while surprisingly others stay at the stage of non-graphitic carbons.[34,35] Those graphene-based carbon materials which do convert into graphite, namely "mesophase pitch" for instance, in essence, can – or need to – be interpreted as "mesocrystals" according to the concept introduced by Helmut Cölfen.[36–38] Since the conversion into graphite requires the parallel mutual arrangement of graphene stacks, and since their dimension commonly is on the nanometer scale, concepts of "non-classical crystallization" must be included for understanding the transition from amorphous to crystalline carbon via the intermediate formation of such "graphene mesocrystals".

Also, the templating of carbons using block copolymers involves questions similar to Cölfen's studies on manipulating biomineralization of basic inorganic compounds by block copolymers: the block copolymer micelles used as templates here might interact with the surrounding carbon precursor and also form carbonaceous species and thereby affect the transformation of amorphous carbon into graphene sheets, i.e., a "crystallization" process.[33,39–41] Thus, we try to elucidate – similar to the polymer-mediated biomineralization and "non-classical crystallization" – the impact of the block copolymers on the carbonization.

Although soft templating is used for preparing mesoporous carbon for 20 years,[42] most studies are restricted to small mesopores below 10 nm achieved with Pluronics polymers,[4,5,7,28,43–46] which might suffer from slow diffusion of reactants through the pore system.[47,48] The step toward larger mesopores of 30–70 nm

comprising a still high surface area and ideally, a less restricted mass flow within the mesopores is possible by using different soft templates such as poly(ethylene oxide)-*block*-poly(styrene) (PEO-*b*-PS),[3,49] poly(styrene)-*block*-poly(4-vinylpyridine) (PS-*b*-P4VP),[42] and poly(ethylene oxide)-*block*-poly(hexyl acrylate) (PEO-*b*-PHA)[50] block copolymers. With the aid of the latter, we recently investigated the pore structure in mesoporous powders of metal oxides,[51] and successfully realized the synthesis and characterization of lignin-derived mesoporous hard carbons with variable pore sizes between 20 and 50 nm, applying soft templates of the PEO-*b*-PHA family.[52] However, these hard carbons possessed only isolated spherical mesopores, which appear to be beneficial for application in sodium-ion batteries[52] but are disadvantageous for electrocatalytic applications, in which pore accessibility for reactants has to be ensured. Otherwise, the catalytic activity decreases consecutively upon lowering the accessibility of the pore structure as recently shown for mesoporous carbon particles prepared from poly(styrene)-*block*-poly(dimethylsiloxane) copolymers.[53]

With regard to electrochemical applications, the synthesis of hard carbons with large mesopores[3,52] has to be combined with a protocol for obtaining mesoporous carbon with accessible pores[9] and then converted to a thin film procedure. Frequently studied carbon materials – typically, derived from phenolic resins – feature an accessible pore system in contrast to the aforementioned lignin-derived carbon and were already prepared in form of a thin film in the past[7,28,42,46] even though pore shape and/or size differed from that targeted here (large spherical mesopores of 70 nm in diameter). In literature, the majority of ordered mesoporous carbon films used as support for electrocatalysis were applied for the cathodic hydrogen evolution reaction (HER) so far but not for the anodic OER counterpart.[7,54] The obvious reason represents the fact that carbon typically gets oxidized to carbon dioxide (and partly carbon monoxide and surface oxygen species as well) if an oxidative (anodic) potential is applied.[55–59] Yet, carbon possesses a large variety in its chemical nature (e.g., graphitic in contrast to non-graphitic carbon), and so, carbon's stability in electrocatalysis differs as well, e.g., with a delayed carbon corrosion in case of graphitized carbon felts (corrosion starting from 1.2 V vs. RHE instead of $E_0 = 0.2$ V).[56,58] Therefore, a resorcinol-derived mesoporous hard carbon thin film might be sufficient to withstand the harsh electrocatalytic conditions of the acidic OER (i.e., pH of 1 and 1.2–1.4 V vs. RHE). By using a self-synthesized PEO_{372}-*b*-PHA_{180} block copolymer as soft template, we successfully prepared both mesoporous powders and thin films with circa 70 nm spherical pores on titanium plates.

Combining secondary ion mass spectrometry, electron microscopy, and X-ray diffraction, the substrate corrosion and strategies to avoid it were explored. Based on thermogravimetry coupled with mass spectrometry, we comprehend how the resin is transformed to the final carbon material while the (also organic) soft template is decomposed. Contrasting these findings to gas physisorption experiments of templated and non-templated carbon powders, we propose a detailed picture of the observed pore system, in which the intrinsic micropores of the resorcinol-derived hard carbon might play a major role in connecting the spherical mesopores. Next to an in-depth characterization of the carbon microstructure of the powder material by Raman spectroscopy and X-ray diffraction, we investigate the resulting properties of the thin film counterpart: While infiltration with a tracing electrolyte reveals insights into pore accessibility, the electric conductivity is studied by impedance spectroscopy and Hall measurements, and the stability under OER conditions is tested by cyclic voltammetry and electron microscopy. By these experiments, we study if mesoporous carbon thin films might fulfill the prerequisites of an electrocatalyst support – namely, an accessible pore system combined with a stable and conductive carbon skeleton, and thus might act as a promising material for electrocatalytic applications like the acidic OER.

2. Results and Discussion

2.1. Synthesis of Mesoporous Carbon

Ordered mesoporous carbon powders and thin films were prepared by a soft templating approach according to Tanaka et al.[9] based on a resorcinol-formaldehyde resin as a carbon precursor. The amphiphilic block copolymer PEO_{372}-*b*-PHA_{180} (subscripts denote the number of repeating units according to the NMR analysis in Figure S1, Supporting Information) applied as soft template was obtained by a supplemental activator reducing agent atom transfer radical polymerization (SARA ATRP) analogue to our recent study.[51] As illustrated in **Figure 2**, resorcinol and the soft template are independently dissolved prior to the combination and addition of triethyl orthoacetate (as pore-stabilizing agent[9]), and an aqueous formaldehyde solution (as cross-linker). For the synthesis of powders, which are required as a reference for deeper structural characterizations, the solution was directly dried in an oven, while for the preparation of the thin films, the reaction mixture was spin-coated on a polished titanium plate (as a conductive substrate) before drying. In both routes, drying at 80 °C promotes acid-catalyzed thermopolymerization of resorcinol and formaldehyde, yielding a resol resin in the space between the soft template.[60–62] The resin is then converted to a non-graphitic carbon (NGC) during the following heating step under an inert gas atmosphere, whereas the soft template is removed. The soft templating process, based in case of both powder and thin film on the evaporation-induced self-assembly (EISA) mechanism:[51,63–65] The block copolymer, which dissolves initially as a statistical coil in ethanol, undergoes micellization upon solvent evaporation (at 80 °C).[51] These micelles arrange themselves in an ordered, closed-packed array during proceeding evaporation and decompose selectively in the anaerobic carbonization step, yielding a mesoporous carbon pattern.

The soft templating procedure is not straightforward as it requires a selective built-down of only one organic phase (soft template) within a second stable one (resin), and the question thus arises if the soft template fully decomposes during the heating procedure. To answer this question, we coupled a thermogravimetric study with mass spectrometry of the released products (TG-MS), which reveals the underlying processes. The TG-MS experiment tells not only which fragments are released at which temperature but is also capable of checking the overall suitability of the heating ramp used in the synthesis, i.e., if the dwell times are properly chosen. Following the TG curves of the pure template, the pure resin, and the reaction mixture containing both (**Figure 3**) along the heating ramp, four steps become apparent: (1) removal of residual solvents and volatile species, (2) extrusion

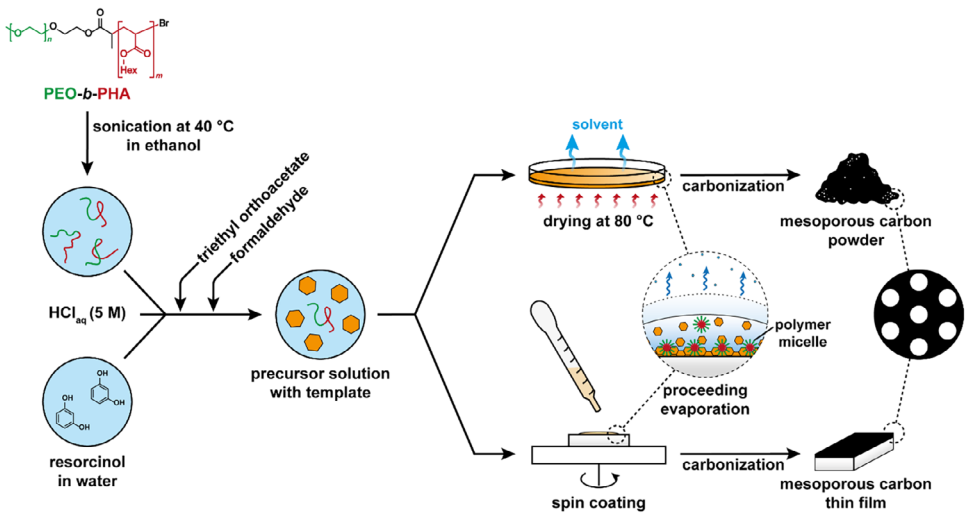

Figure 2. Overview on the synthesis of mesoporous carbon powders and thin films from resorcinol-formaldehyde (resol) resins with poly(ethylene oxide)-*block*-poly(hexyl acrylate) as soft template.

of water (by further condensation), (3) template decomposition, and (4) heteroatom removal during carbonization.

Until ≈200 °C (below 175 min), a mass loss of 10% (reaction mixture) and 12% (pure resin) is detected, which can be attributed to solvent removal following the MS signal of the water radical cations (m/z = 18) and the ethanol fragments (e.g., m/z = 31). In the case of ethanol, the fragment ion with m/z = 31 (protonated formaldehyde) is more reliable than the ion with m/z = 27 (ethylene cation), which also shows an increased intensity below 200 °C but could be confused with the ethylene cation released from the PHA block according to the fragmentation pattern in Scheme S1 (Supporting Information). Additionally, the release of residual formaldehyde (m/z = 30) can be found in this regime at ≈80 °C (see pure resol scan in Figure S2B, Supporting Information). Starting from 200 °C (after 175 min), a second water release step occurs (m/z = 18), which can be attributed to further condensation reaction in the resol resin. Indeed, ^{13}C-NMR studies of Meng et al. confirm further cross-linking in phenolic resins below 350 °C.[60] These yield a mass loss of circa 16% (reaction mixture) and 23% (pure resin), respectively. However, in the case of the reaction mixture, this step overlaps with the decomposition of the soft template (circa 18% mass loss) starting from 300 °C (275 min). The choice of unambiguous tracing ions indicating template removal arises from the proposed fragmentation pattern in Scheme S1 (Supporting Information) and is confirmed by the individual TG-MS scan of the pure template in Figure S2A (Supporting Information): Following a thermal depolymerization of the PHA block and subsequent electron impact ionization, a hexyl acrylate cation is formed, which can be built down to either a hexyl cation (m/z = 85) or an ethylene cation (m/z = 27). Both ions are clearly detectable (Figure S2A, Supporting Information) and possess an almost identical intensity evolution (both position and shape) during heating. Thus, a common source of both ions, such as the PHA block built down, is reasonable rendering these ions suitable for tracking the PHA block decomposition. The PEO block can be combusted according to two mechanisms shown in Scheme S1 (Supporting Information): either a thermal depolymerization releasing ethylene oxide cations (m/z = 44) or via α-C–H transfers[66] yielding several small aldehydes and alcohols. Among these, the generated ethanol produces the same fragment ions as the solvent before, which is the reason why an ion with m/z = 31 is observed next to the ethylene oxide cation (m/z = 44) in Figure S2A (Supporting Information) and Figure 3. Due to PEO's hygroscopic character, a water release (m/z = 18) can be detected during PEO decomposition. Since this signal is also found in the scan of the pure soft template (Figure S2A, Supporting Information), this ion can be assigned to the polymer and not to further resin cross-linking in Figure 3. Also, the intensity evolution of signals 44, 31, and 18 are all centered at 390 °C (Figure S2A, Supporting Information), hinting at a common source. From this individual scan, it becomes apparent that PEO decomposes slightly (≈10 °C) before the PHA block. Regarding the scan of the reaction mixture in Figure 3, both PEO and PHA combustion can be confirmed while monitoring the PEO fragments (m/z = 44 and m/z = 31), parallel water release from hydrophilic PEO (m/z = 18), and PHA fragments (m/z = 27), indicating removal of the entire template (both polymer blocks). A final mass loss of 14% (reaction mixture) and 19% (pure resin) starting from 450 °C (605 min) can be assigned to heteroatom removal from the resin following the cations m/z = 44 and m/z = 18 as shown in the fragmentation pattern in Scheme S1 (Supporting Information). Such further cross-linking of the aromatic benzene rings at higher temperatures is in alignment with ^{13}C-NMR and infrared spectra in the literature.[60]

A quantitative consideration of the mass losses is challenging because the starting composition (exact mass ratio of polymer to resin) used for TG-MS (after drying at 80 °C) is unknown. A semi-quantitative comparison between the reaction mixture and pure resin, however, is possible if a normalization on the first or last mass loss is performed (**Table 1**).

Normalizing on the first mass loss (10%) of the reaction mixture (last column in Table 1), which is especially in the case of the pure resin, relatively well separated from the pronounced condensation step, the 14% loss in the mixture is contrasted to 16% (initially 19%) mass loss in the pure resin. This suggests a more advanced heteroatom removal in the non-templated

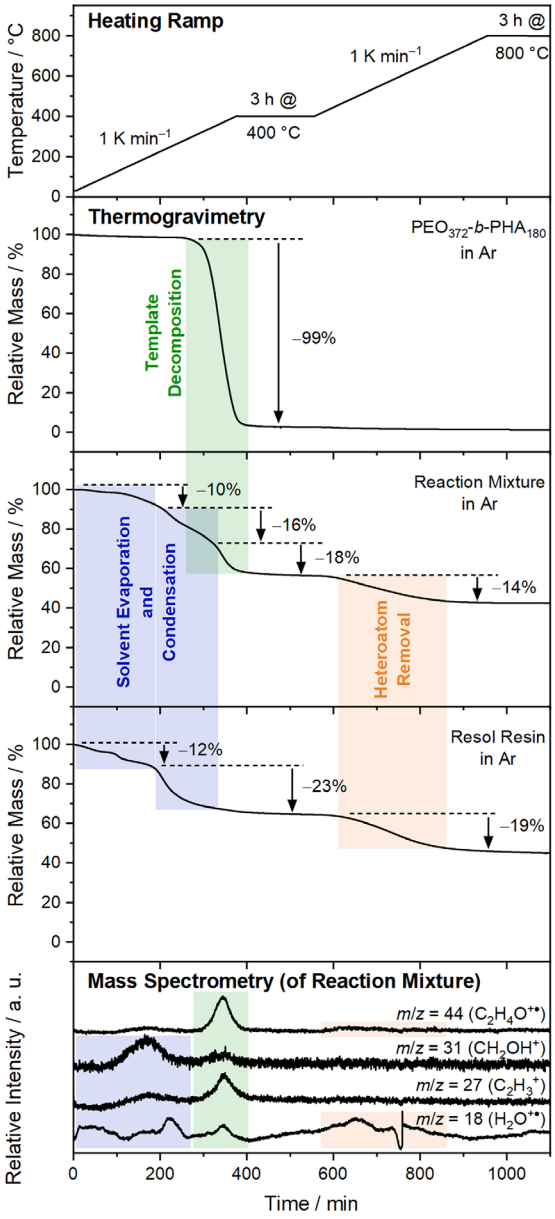

Figure 3. (Middle) Thermogravimetric analysis of the pure soft template, the reaction mixture, and the reaction mixture without soft template (pure resol resin) measured in argon following (top) the heating ramp used for the synthesis. In addition, (bottom) the evolution of the MS signals related to the release of water, ethanol, ethylene oxide, and PHA fragments from the reaction mixture are displayed, and processes describing solvent evaporation and condensation reactions (blue), polymer decomposition (green), and heteroatom removal during carbonization (orange) are highlighted.

sample, which is in alignment with our recent study.[52] Also, kinetic studies of Vogt and co-workers derived from infrared spectroscopy confirm a delayed cross-linking of the resin in the presence of a soft template.[10] However, a mass loss of ≈18% in the reaction mixture connected to polymer decomposition (second column in Table 1) hints at an incomplete template removal since a value of 25 – 37% is expected. This expected value derives from

Table 1. Observed mass losses of the templated (meso) and non-templated sample (dense) according to thermogravimetry during (1) solvent evaporation, (2) condensation, (3) template removal, and (4) carbonization. Additionally, these experimental values are normalized to the mass loss of the dense sample during carbonization (fourth column) and to the mass loss of the mesoporous sample during solvent evaporation (fifth column) for comparison.

	observed Δm_{rel}		corrected Δm_{rel}	
step	meso	dense	meso	dense
(1)	–10%	–12%	–14%	–10%
(2)	–16%	–23%	–22%	–19%
(3)	–18%	–	–24%	–
(4)	–14%	–19%	–19%	–16%

a gravimetric consideration if the weight fraction of all components in the initial reaction mixture is regarded (**Figure 4**). Following the recipe of a mesoporous powder in the experimental section, the soft template contributes 4.4 wt.% to the mixture. Assuming that ethanol, water, the aqueous formaldehyde solution, and the 5 M hydrochloric acid (composed of 0.7 wt.% water and 0.1 wt.% HCl compared to the entire mixture) represent volatile components during drying at 80 °C, 82.3 wt.% of the mixture's mass are removed while 17.7 wt.% remain in the resin residue after drying. The share of the soft template to the mixture is thus increased to 25% after removal of the volatile species (4.4 wt.% vs. 17.7 wt.%). In the actual synthesis, the weight of the mixture after drying dropped even stronger than the expected values in Figure 4. Both the batch with and without soft template experienced a weight loss being 5 wt.% higher although residual solvent is still present in the resin according to TG-MS (Figure 3). The reason might be the release of water during thermopolymerization and thus condensation of resorcinol and formaldehyde.[62] Consequently, the share of soft template in the resin could increase to even 37% (4.4 wt.% vs. 12.0 wt.%) yielding overall the aforementioned expected mass loss of 25–37%. Even though this argumentation claims soft template residues to be present in the final NGC (or a fraction of template being carbonized as well), an (at least partly) degradation of both blocks can be clearly concluded. Yet, NMR studies in literature demonstrated that PEO can be entirely decomposed within a phenolic resin.[60]

Alternatively, if a similar carbonization behavior in both samples is assumed, i.e., normalization on the last mass loss (of 19%) of the pure resin (third column in Table 1), 24% (initially 18%) of mass is lost due to the soft template suggesting a full template removal if compared to the theoretical values discussed above. In summary, the analysis of the TG curves leads to the interpretation that either carbonization is less advanced while template residues might be present or that the soft template is fully removed, assuming a similarly advanced carbonization of the NGC skeleton in both the non-templated and mesoporous carbon. Although the question of a quantitative template removal cannot be answered accurately, this TG-MS study still confirms the suitability of the heating ramp as a plateau is reached both after template and after heteroatom removal, implying that longer heating steps would not lead to further improvements.

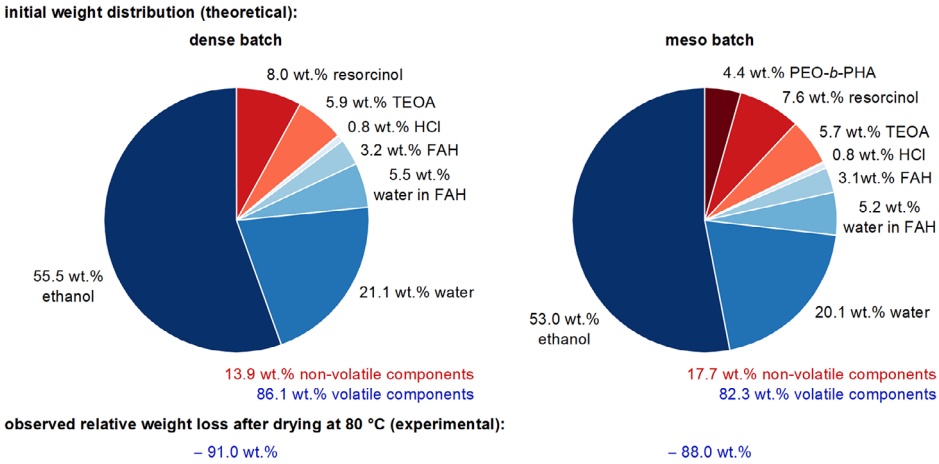

Figure 4. Weight distribution of all components in the synthesis of (left) non-templated and (right) soft-templated carbon according to the protocol in the experimental section, with TEOA describing triethyl orthoacetate, HCl describing hydrochloric acid, and FAH describing an aqueous formaldehyde solution. All non-volatile species are displayed in red colors, while volatile components are shown in blue. In addition, the relative mass loss from starting the reaction to the resin residue after drying is given at the bottom each.

2.2. Carbon Microstructure

Verifying the presence of graphene stacks formed during carbonization (at 800 °C) and required for electric conductivity, and a possibly larger extent of these stacks in the non-templated sample requires a detailed carbon microstructure analysis. The electron image in **Figure** 5A obtained by transmission electron microscopy (TEM) confirms that graphene stacks are present in the mesoporous carbon powder at a local level, but a statistical and reliable interpretation at a global level is only possible by other methods. In this regard, Raman spectroscopy can help to give a first statement. However, due to the small sample quantity in a thin film, this characterization is restricted to the powder state. Both samples possess a pronounced D (≈1340 cm^{-1}) and G band (≈1590 cm^{-1}) in the Raman spectra (Figure 5C) as well as the typical overtones between 2500 and 3000 cm^{-1} frequently observed in non-graphitic carbon.[52,67–70]

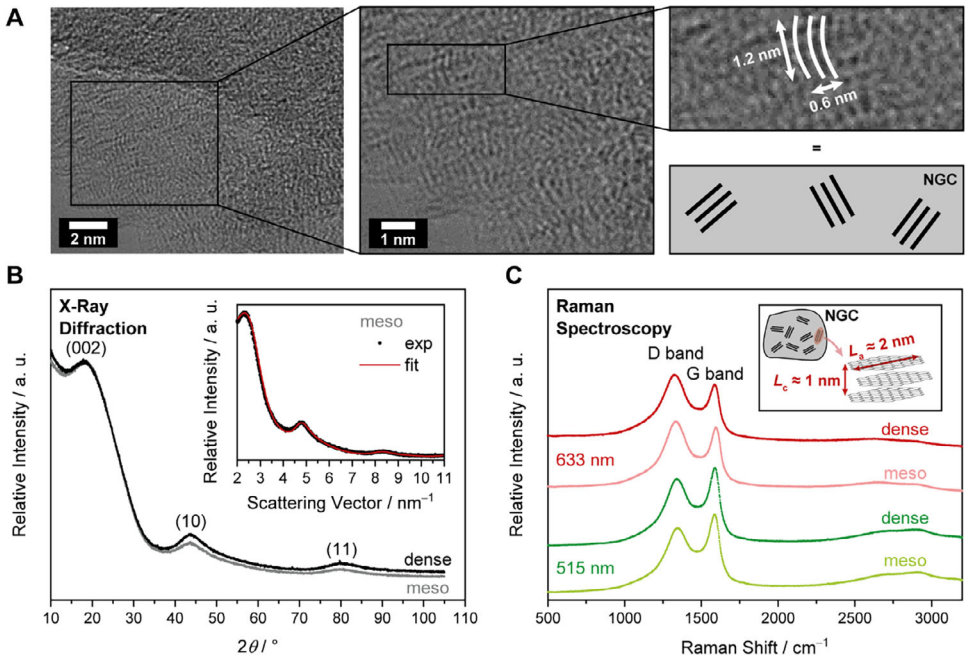

Figure 5. A) TEM image of mesoporous carbon powder with an exemplary graphene stack highlighted in white; the microstructure of this non-graphitic carbon (NGC) is sketched underneath. B) XRD patterns of non-templated (black) and mesoporous (gray) carbon powder (black) carbonized at 800 °C, as well as a fit of the latter according to an algorithm based on Ruland and Smarsly (ref.[76]) in the inset. C) Raman spectra of the non-templated (dark color) and mesoporous powder (light color) measured with an excitation wavelength of 633 nm (red) and 515 nm (green) shown with a scheme of an average graphene stack in NGC based on the XRD and Raman spectroscopy results in the inset.

The presence of the graphitic lattice mode (G band) and the defect-based D1 band already confirms the presence of graphene stacks, but their evaluation is only possible by a deconvolution of the overlapping D4, D1, D3, and G band (the D2 band is not expected here due to the comparably low carbonization temperature[52,69,71,72]). Applying two excitation wavelengths (633 and 515 nm) bakes up the evaluation as multiple correlation curves can be used for determining the intensity ratio of the D1 to the G band.[67] The deconvolution (Figure S3, Supporting Information) yields the D1 and G band position (633 nm) as well as the intensity ratio of the D1 to the G band $I_{D1}\ I_G^{-1}$ (both 633 and 515 nm), from which the extent of the graphene sheets can be estimated by comparison with the empirical correlation curves of Schuepfer et al.[67] and Osswald et al.[72] shown in Figure S4 (Supporting Information). Comparing the non-templated (dense) sample with the mesoporous one, the G band is slightly shifted to larger wavenumbers while the D1 band is shifted to smaller values; also, the intensity ratio $I_{D1}\ I_G^{-1}$ is a bit higher. All these trends hint at a slightly larger layer extent in case of the non-templated sample. The larger graphene sheet extent in the non-templated powder confirms the assumption of a lower heteroatom removal drawn from TG-MS and is in alignment with our previous study[52] on lignin-derived hard carbons. In absolute values, however, the effect is rather small: Depending on the applied correlation curve, an average graphene layer extent L_a of 2.5–3.5 nm is obtained (see Table S1, Supporting Information) with the dense sample possessing a slightly larger L_a value (by 0.1–0.2 nm). Yet, a recent wide-angle neutron scattering study showed that the correlation curve in Figure S4A (Supporting Information) overestimated L_a,[72] and a value of 1.3 nm might be more reasonable. Generally, the Raman-based estimation is affected by two major drawbacks: (1) Defects influence the Raman spectrum and thus, the regarded correlations depend on the applied carbon precursor.[67] This becomes particularly apparent from the deviation of the empirical values from the calibration curve in Figure S4C (Supporting Information) and the difference between pitch- and resin-based carbons[67] hampering the evaluation of the 515 nm spectra. (2) Furthermore, the correlation curves of G band position and intensity ratio are not universal, i.e., yield two L_a values in most cases. In this work, the smaller layer extent of 1.5–3.5 nm is rather obviously preferred over the large one beyond 8 nm according to comparable carbon samples in literature prepared at a low carbonization temperature (800 °C), resulting in ≈2 nm graphene layers.[52,67] Additionally, the TEM image in Figure 5A shows only occasionally small graphene stacks of L_a = 1.5 nm in diameter, supporting this theory. Nevertheless, the graphene layer extent from Raman spectroscopy possesses a large uncertainty and hence needs further confirmation.

Wide-angle X-ray scattering (WAXS), therefore, is a powerful tool to not only validate the Raman-based L_a value but also to gain deeper insights into various microstructure parameters of such turbostratic carbons.[73,74] By fitting the WAXS data with an algorithm based on Ruland and Smarsly[74] with the aid of the *OctCarb* script[75] and the GNU *Octave* software,[76] the average graphene layer extent L_a, the average interlayer spacing a_3, and the average stack height L_c can be determined among others (Table S2, Supporting Information). Doing that, the WAXS data in Figure 5B comprising the (002) reflection from inter- as well as the (10) and (11) reflection from intralayer scattering can be fitted as shown in the inset for the mesoporous powder (and Figure S5, Supporting Information for the non-templated sample), which delivers slightly more advanced graphene stacks in the non-templated carbon with L_a = 1.9 nm (vs. mesoporous carbon: L_a = 1.8 nm), a_3 = 0.37 nm (meso: 0.37 nm), and L_c = 0.74 nm (meso: 0.84 nm). Thus, the aforementioned hypothesis of a slightly restricted carbonization due to soft templating is confirmed, as well as the presence of nano-sized graphene stacks in both samples. In conclusion, graphene stacks of ≈2 nm in width and 1 nm in height can be found in this non-graphitic carbon, corresponding to the illustrated stack in the inset of Figure 5B and agreeing with both the example in the TEM image in Figure 5A and comparable samples in literature[52,67] carbonized at 800 °C. These graphene stacks play an important role in introducing electric conductivity into the material and thus are necessary for an application as an electrocatalyst support.

2.3. Morphological Investigation of the Mesopore Structure

So far, the carbon microstructure has been intensively investigated, but not the targeted mesoporous morphology. Concerning the powder sample, several characterization tools are applicable such as (scanning and transmission) electron microscopy (SEM and TEM) and gas physisorption. Both the SEM and TEM image in **Figure 6A** and B reveal an ordered pore system with spherical pores of 60 nm in diameter. Taking our previous studies of PEO-*b*-PHA-derived metal oxides[51] and carbon[52] into account, pore size and shape observed in this work are in good agreement with the previous works. The fact that the TEM-based pore size is slightly larger than the SEM-based one – although still being within the experimental error comparable – might be due to a systematic underestimation of SEM-derived pore sizes because the breaking plane resulting in the spherical cavities at the surface (observed in Figure 6A) in most cases does not cut the spherical pore along the center, i.e., along the maximum perimeter.

In contrast to a thin film, a powder sample enables a precise physisorption measurement, drawing a global picture of the pore structure. The nitrogen isotherm (Figure 6C) supports the presence of a mesoporous material according to the hysteresis loop. Although a significant cavitation phenomenon becomes apparent, claiming a poor pore accessibility through narrow bottlenecks analogous to comparable silica powders,[51] the significant mesopore volume confirms that the mesopore network is accessible at all in difference to comparable lignin-derived carbons.[52] Furthermore, the isotherm states that a significant number of micropores is present as well, which could be assigned to micropore channels induced by PEO single chains similar to mesoporous silica samples.[51] However, a comparison with the nitrogen isotherm of the non-templated carbon powder (black dots in Figure 6C) evokes the hypothesis that these micropores originate from intrinsic cracks of the hard carbon. These intrinsic micropores featuring a larger surface area than mesopores of the same pore volume also explain the higher specific surface area of the non-templated sample compared to the mesoporous one in Figure 6C. The micropore volume of both powders matches almost perfectly, whereas lignin-derived hard carbons do not possess any (accessible) microporosity if prepared

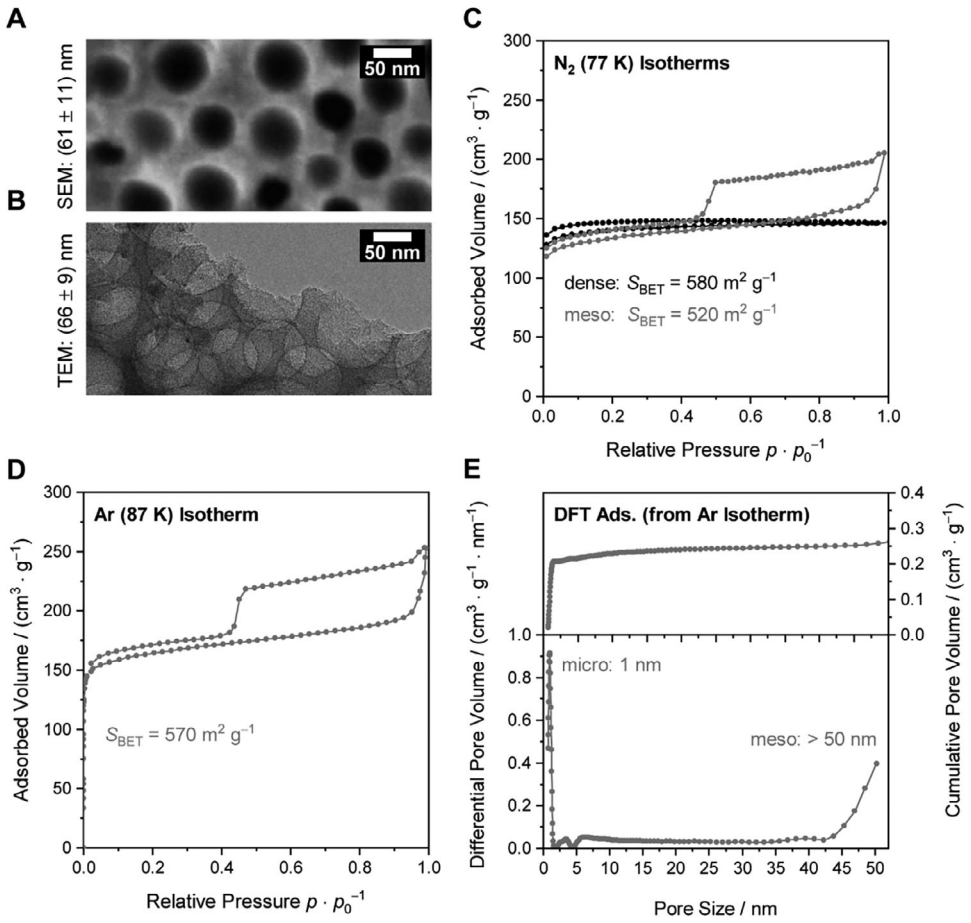

Figure 6. A) SEM and B) TEM image of mesoporous carbon powder. In addition, C) the nitrogen isotherms at 77 K of the mesoporous powder (gray) is contrasted to that of the non-templated (dense) one (black). The D) argon isotherm at 87 K of the mesoporous sample and (E) the corresponding pore size distribution obtained from the adsorption branch applying a QSDFT hybrid kernel for cylindrical/spherical pores are shown for deeper pore analysis as well.

without a soft template.[52] If prepared in a mesoporous fashion, different amounts of microporosity are observed by physisorption depending on the template used to prepare these lignin-derived carbons.[52] Still, the MS signal ($m/z = 44$) in Figure 3 clearly confirms a PEO decomposition here, which is in alignment with NMR studies of resin-derived carbons in literature,[60] but apparently does not increase the micropore volume per gram carbon compared to the non-templated reference powder. This contradiction can be resolved by the templating model sketched in **Figure 7**: Upon heating at 80 °C, the solvent evaporates while cross-linking of the carbon precursor takes place simultaneously. As a result, a closely packed pattern of polymer micelles forms,

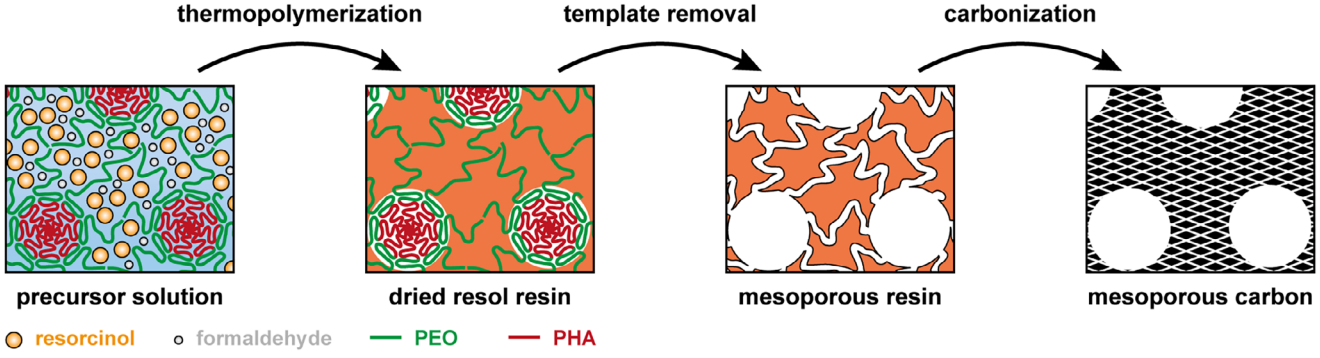

Figure 7. Schematic evolution of the pore structure during template removal and carbonization converting template-based micropores to intrinsic micropores.

embedded in the resol resin. During the first heating ramp under inert atmosphere, the soft template is removed (see TG-MS study in Figure 3), yielding a pore structure in which mesopores are connected by micropore channels. This situation depicted in the third image of Figure 7, represents the pore structure of amorphous mesoporous silica.[51] Increasing the temperature even further leads to a collapse of these micropores, while intrinsic micropores are formed during carbonization. These intrinsic micropores are often interpreted as voids between graphene stacks according to a house-of-cards model,[77–79] and indeed, a significant microporosity is frequently observed in comparable hard carbons.[3,60] Consequently, a homogeneously microporous carbon skeleton is obtained, explaining the same amount of micropore volume in the mesoporous carbon as for the non-templated powder. This represents a major difference to lignin-derived hard carbons and might explain the presence of isolated mesopores in them while applying a comparable PEO-*b*-PHA copolymer as soft template. If this carbon precursor system intrinsically does not form a comparable high number of micropores as phenolic resins, which might be responsible for connection and thus accessibility of the large mesopores, an isolated (meso)pore system is obtained. Note that the schematic representation in Figure 7 focuses on the evolution of the micropores during heating and does no state that all mesopores are only connected by micropores, as shown here. The possibility of mesopore connection through larger mesopore windows derived from micelle overlapping observed in silica[51] might also occur here as well.

In order to determine the pore size by physisorption, a detailed argon isotherm was recorded at 87 K (Figure 6D). The presence of micropores of 1 nm in size is clearly confirmed by the DFT-based pore size distribution in Figure 6E, which also reveals the presence of larger cavities above 40 nm in diameter. Although the QSDFT hybrid kernel applied on the adsorption branch is expected to be particularly suitable for spherical mesopores connected by cylindrical micropores,[80] an accurate pore size determination is challenging in this case because current QSDFT evaluation models have been programmed for pore sizes only up to 50 nm yet. Hence, a mode pore size above 50 nm can be concluded to be in alignment with electron microscopy, but an exact value cannot be given with this method here.

2.4. Substrate Corrosion in Mesoporous Carbon Thin Films

Transferring the powder synthesis to mesoporous carbon thin films requires spin coating of the same precursor solution onto a defined substrate. When using a titanium plate as substrate, which is necessary in electrocatalysis to ensure electric contact, however, bright tarnished spots are obtained on the otherwise deep black carbon coating (expected for non-graphitic carbon) after carbonization in a tube furnace with continuous argon flux. The surface scans in Figure S6 (Supporting Information) acquired by secondary ion mass spectrometry (SIMS) confirm the presence of titanium oxide species on the surface. The overlay of the C_4^- (m/z = 48.00) and TiO_2^- (m/z = 79.94) ion signals clearly demonstrates the presence of two separated phases: the non-graphitic carbon and a titanium species – possibly titanium oxide. Also, if a blank, polished Ti substrate without any carbon coating is annealed under analogous conditions, a tarnished surface is obtained, yielding fragment ions composed of titanium and oxygen in SIMS (Figure S6, Supporting Information). Since SIMS only provides information on the elemental composition, an assignment of the actual phases remains unclear. For this reason, X-ray diffraction under grazing incidence (GIXRD) of the annealed substrate and the mesoporous carbon film is needed to understand the origin of the titanium species. The GIXRD patterns in Figure S6 (Supporting Information) unambiguously show the expected occurrence of substrate-related reflections (e.g., the main reflection of Ti metal at $2\theta = 40°$) as well as the presence of TiO_2 (rutile structure), as can be seen from the reflections at $2\theta = 27°$ and 54° in both the annealed substrate and the carbon thin film. The carbon phase almost drowns out due to the little amount of carbon and the low scattering intensity of the rather amorphous NGC phase. A small background observed in XRD around $2\theta = 20°$ can be assigned to the carbon coating. These experiments strongly hint that the corrosion of the Ti substrate (i.e., formation of TiO_2) is responsible for the surface impurity leading to the tarnished appearance of the thin films. Several attempts were investigated to mitigate this corrosion, and we discovered that the introduction of 15 vol.% of carbon monoxide to the inert feed gas during carbonization was sufficient to prevent the formation of oxide particles (see the Supporting Information for more details). When carbonized in such an Ar/CO mixture, neither TiO_2-related ions are found by SIMS nor corresponding reflections by GIXRD (Figure S6, Supporting Information). While SIMS confirms the surface to be composed solely of non-graphitic carbon, the GIXRD pattern features, in addition to Ti-related reflections, several signals that can be assigned to titanium carbide (located at 2θ = 36, 42, and 60°). These can be found in the pattern of the carbon film carbonized in pure argon as well, but the absence of Ti-containing ions in the SIMS surface scan of the apparently non-corroded thin film raises the question where TiC is located. To tackle this question, depth profiles of the mesoporous carbon thin films carbonized in pure Ar and the Ar/CO mixture, respectively, were recorded by SIMS (**Figure 8A,B**). Here, the intensity profiles of all mass signals were normalized and stacked for a better overview.

In case of the thin film carbonized in pure argon (Figure 8A), many titanium/oxygen species like TiO^- and TiO_2^- (but also TiO_3^- in Figure S17A, Supporting Information) and heavy carbon fragments like C_4^- (and also C_7^- in Figure S17A, Supporting Information) can be found near the surface. Overall, the intensity evolution of the carbon- and titania-based ions shows a comparable sigmoidal trend of a decay ≈700 nm in depth upon ongoing sputtering. Yet, a small deviation between these two kinds of fragments becomes apparent between 400 and 600 nm with an increase in carbon-based signal intensity next to a small decrease in titania-based signal intensity. This observation can be explained with TiO_2 particles on the former surface of the thin film (see SEM images in **Figure 9**; Figures S8,S9, and S13, Supporting Information) leading to a relative enrichment of titania-derived ions at the (former) surface and a relative enrichment of carbon-based signals underneath the (former) surface after sputtering through these surface particles and reaching the actual carbon film. Generally, the evolution of the signal's intensities claims for a surface layer composed of hard carbon and TiO_2 with the latter being the dominating species. After further sputtering (> 600 nm), the aforementioned signals become weaker whereas

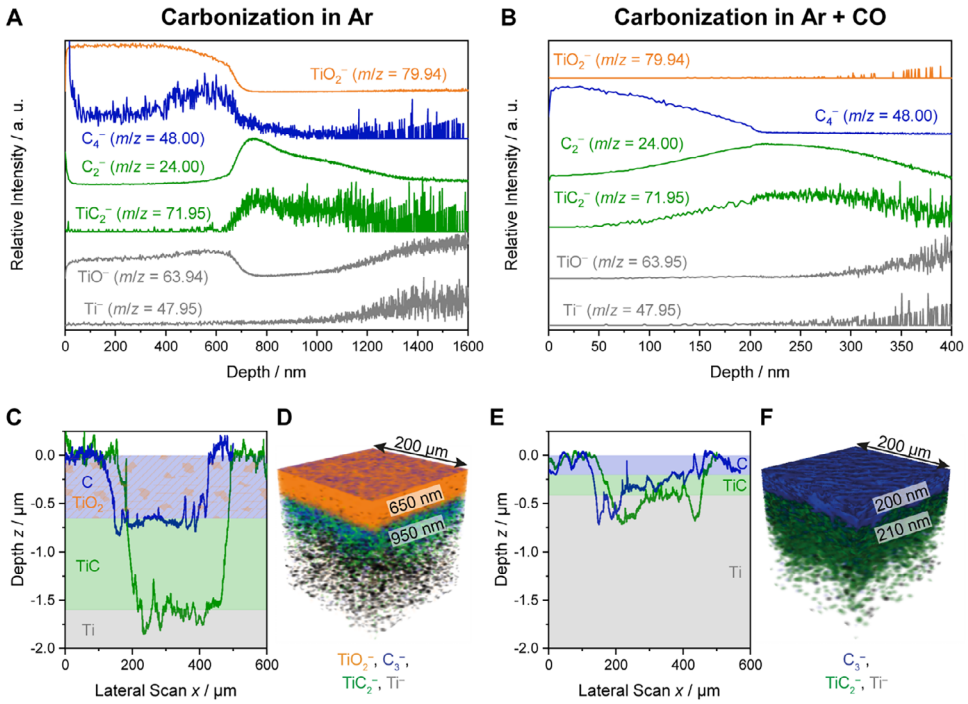

Figure 8. SIMS depth profiles of mesoporous carbon thin films on titanium substrates carbonized in A) pure argon and B) a mixture of 85 vol.% argon and 15 vol.% CO comprising the evolution of the ion signals assigned to the TiO_2 phase (in orange), the hard carbon phase (in blue), the TiC phase (in green), and the metal substrate (in gray) with proceeding sputtering. The (C and E) AFM scans of the sputter craters before reaching the TiC interphase (blue) and the metal substrate (green), respectively, are given as well as the (D and F) 3D overlay of the TiO_2^-, C_3^-, TiC_2^-, and Ti^- signal with the respective layer thickness from AFM.

the ion signals of lighter carbon fragments like C_2^- (and also C_3^- in Figure S17A, Supporting Information) and titanium/carbon species like TiC_2^- (and also TiC^- in Figure S17A, Supporting Information) become more intense. The parallel intensity trend of these two kinds of fragments hint at the appearance of the TiC phase observed by GIXRD (Figure S6, Supporting Information). Moreover, the opposed intensity evolution of the light vs. the heavy carbon fragments evokes the hypothesis that non-graphitic carbon, possessing small graphene stacks (see Figure 5), decomposes preferentially into larger carbon species while the carbide only forms small carbon anions (see Figure S17C, Supporting Information). This might be reasonable since larger carbon species most likely are more challenging to from starting from the rock salt structure of TiC than from a large carbon network, i.e., a non-graphitic carbon containing aromatic ring structures. For depths > 1200 nm, the TiC-related ion signals become less intense or at least their signal noise increases in parallel to an increase of the TiO^- and Ti^- ion count, which can be assigned to the crossing of the TiC/Ti interface and a penetration of the metallic substrate. Consequently, a mixed C/TiO_2 surface layer and a TiC interphase on top of the metallic substrate can be concluded from the depth profiles in Figure 8A, which becomes obvious in the 3D overlay of the TiO_2^-, C_3^-, TiC_2^-, and Ti^- ion signals in Figure 8D, confirming a layered structure. The thickness of the respective layers requires an additional measurement. The atomic force microscope (AFM) implemented in the SIMS setup enables topographic analyses of the created sputter craters. When sputtering is stopped at the inflection point of the signal intensity evolution (e.g., the TiO_2^- signal evolution), the sputter crater can be assumed to end at the interface between two phases. Thus, the two depth profiles in Figure S17A,C (Supporting Information) correspond to sputter craters terminating at the interface between the C/TiO_2 and TiC phases and the interface between TiC and the substrate, respectively. The corresponding height profiles of the sputter craters obtained from AFM in Figure 8C give access to the layer thickness by measuring the height difference each. As a result, the fluence (sputter ion exposure) can be converted to the depth (*x*-axis) in Figure 8A and B (since the sputter rate of each layer is known through the measured layer thickness), and an overall structure of a 650 nm thick C/TiO_2 surface layer above a 950 nm thick TiC interphase is obtained for the corroded sample.

The carbon thin film carbonized in an Ar/CO mixture, however, gives no indication of any TiO_2 at the surface (Figure 8B), which can be concluded from the initial absence of TiO^- and TiO_2^- ions. On the contrary, only carbon-based fragments can be found (C_3^-, C_4^-, and C_7^- in Figure S17B, Supporting Information) following all the same trend. Surprisingly, the C_3^- signal follows the trend of the heavier carbon fragments and not that of the carbide-derived ones as observed in the corroded sample in Figure 8A. Apparently, the ionizability of this ion is significantly increased by the absence of TiO_2 in the hard carbon matrix. Underneath the carbon phase at 200 nm, the evolution of the observed ion signals is very similar to those in the corroded sample. Thus, a pure hard carbon phase on the titanium substrate with a TiC interphase between them, possessing again a layered structure (see the 3D overlay in Figure 8F) can be concluded by this SIMS analysis. Performing a similar AFM study of the sputter craters leads to strikingly thinner layers

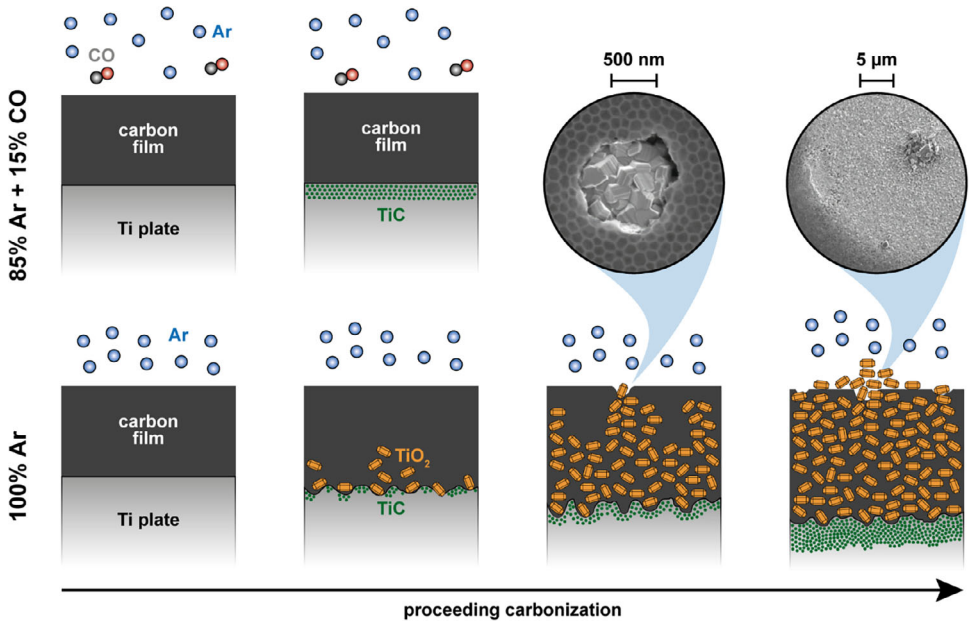

Figure 9. Proposed corrosion mechanism of the titanium substrate if no reducing agent is mixed to the inert feed gas (below) including two SEM images of the titanium oxide particles. In case of an Ar/CO atmosphere (top), only a thin TiC interphase is formed.

compared to the corroded sample: a 200–300 nm thick hard carbon thin film above a 210 nm thick TiC interphase is observed. Measuring the film thickness of the carbon layer is hampered by the crack at a lateral position of ≈200 µm (blue profile in Figure 8E) but from the remaining crater, a thickness between 200 and 300 nm can be concluded, which is confirmed qualitatively by SEM of the cross-section of an analogous carbon film on silicon yielding a thickness between 300 and 400 nm (see below). The reliability of the AFM scans is supported by monitoring the depth profile in the forward and backward direction being in good alignment as shown in Figure S18 (Supporting Information).

The reason that both the mesoporous carbon film and the TiC interphase are tremendously thinner may be the absence of the substrate corrosion by TiO_2 formation. As shown in Figure 9, the oxide forms in the shape of nano-sized particles, and according to the proposed corrosion mechanism, their formation roughens the substrate surface, which makes it more prone to the formation of carbide at the interface. Combining the results from SIMS and the synthesis optimization in the Supporting Information, oxygen traces (from either the feed gas or – more likely – the metal substrate containing 0.25% oxygen according to the supplier) cause the formation of TiO_2 at the metal surface during carbonization. These oxide particles grow through the carbon matrix, break through the surface, and spill over the thin film surface like a volcanic eruption. This coverage of the sample surface with TiO_2 could explain the shape of the C_4^--depth profile in Figure 8A possessing a maximum at ≈500 nm. After sputtering the surficial oxide particles embedding some residual carbon, the actual hard carbon layer (≈300 to 400 nm estimated from the depth profile) infiltrated with TiO_2 is uncovered, showing a similar film thickness as the non-corroded thin film. If a sufficient amount (15 vol.%) of CO as a reducing agent is introduced to the feed gas, the TiO_2 formation is inhibited, the flat carbon film is allowed to carbonize without perturbation, and a homogeneously thin TiC interphase is built at the interface.

To ensure that the introduction of CO into the inert atmosphere does not change the chemical nature of the non-graphitic carbon, mesoporous carbon powders were prepared under different carbonization atmospheres. As shown in Figure S19A (Supporting Information), the XRD patterns look alike irrespective of the resin was carbonized in nitrogen (muffle oven), argon, or a mixture of 85 vol.% argon and 15 vol.% CO (both tube furnace). Consequently, the choice of inert gas does not affect the microstructure of the non-graphitic carbon. To elucidate if possible changes in oxygen content occur when CO is employed as reducing agent, a dried resin and two carbon powders obtained from it after carbonization in pure argon and a Ar/CO mixture, respectively, were analyzed by X-ray photoelectron spectroscopy (XPS). The spectra in Figure S19 (Supporting Information) confirm the expected heteroatom removal upon carbonization leading to an decrease in oxygen content from 24 at.% to 14 at.% (Ar) and 15 at.% (Ar + CO), respectively. However, the elemental composition of both carbonized materials is very similar so that no influence of the CO introduction can be found. Also, this experiment demonstrates that the beneficial role of CO during corrosion inhibition is not due to the direct reduction of the resin but rather due to trapping of oxygen traces before they can react with the titanium metal. Consequently, there is no indication that CO chemically influences the non-graphitic carbon and solely prevents the substrate from being oxidized.

The general formation of titanium carbide at the interface between resin and metal substrate is not surprising if the phase diagram of carbon and titanium is taken into account. At high temperatures like 800 °C, the formation of TiC is thermodynamically expected.[81,82] Yet, the question remains whether this TiC interphase impedes the electrocatalytic application of the mesoporous carbon thin film carbonized in an Ar/CO mixture –, e.g., if the

interphase acts as electric insulator. Indeed, TiC is considered as a good electric conductor and thus is investigated as supercapacitor and electrocatalyst support itself.[83–85] However, to check the suitability of the proposed thin film prepared on a metal substrate for later applications, the electric conductivity, electrochemical stability, and pore accessibility need to be studied in more detail.

2.5. Properties of Mesoporous Carbon Thin Films

Summing up, the successful synthesis of a flat and ordered-mesoporous hard carbon thin film with nano-sized graphene stacks (microstructure in Figure 5), a film thickness of 200–300 nm, and 70 nm spherical mesopores (Figure 9 and see below) was shown. Yet, for application as electrocatalyst support, the carbon thin film must fulfil the following features: (1) the carbon layer has to be electrically conductive, (2) the film has to withstand harsh electrocatalytic conditions (e.g., pH 1 and 1.2 V anodic potential in OER), and (3) the mesoporous network has to be accessible for catalyst deposition and the catalysis in general.

2.5.1. Electric Transport

In order to investigate the electric transport through the non-graphitic carbon, we measured the in-plane resistance (along the surface) of the mesoporous carbon thin film and the transport through the carbon thin film (perpendicular to the surface) and the respective substrate (both a titanium plate and a silicon wafer). While the first measurement provides information on the electric properties of only the thin film, the latter includes coating and substrate (and possible interfaces), providing a figure of merit for the actual electrocatalytic application, in which the sample is contacted from the backside. As an internal benchmark, the carbon film is compared with an analogously mesoporous iridium dioxide (IrO_2) thin film – a typical electrocatalyst for acidic OER.[86–92] The IrO_2 thin film was synthesized (both on silicon and titanium substrates) with the same soft template employed for the carbon analogue, following usual sol-gel procedures[51,92] for metal oxide thin films modified in terms of solvents to ensure micellization of PEO-*b*-PHA[50] (see Experimental Section). The GIXRD data in Figure S20A (Supporting Information) show the main reflections of IrO_2 (at $2\theta = 28$ and 35°) in agreement with the depicted reference pattern although their intensity is rather low and overshadowed by the substrate's reflections due to the small quantity of sample and the low crystallinity after calcination at 350 °C.[92] Similarly, the Raman spectrum (Figure S20B, Supporting Information) confirms the presence of IrO_2 because the expected E_g band (at 570 cm^{-1}), B_{2g}, and A_{1g} (both overlapping at 750 cm^{-1}) are observed.[93] The mesoporous morphology is verified by SEM (Figure S20C, Supporting Information), revealing spherical pores of 79 nm in diameter similar to those in the carbon sample. Compared to the latter, the metal oxide thin film is noticeably thinner, with a film thickness of 48 nm according to ellipsometry. The X-ray reflectometry (XRR) scan (Figure S20D, Supporting Information) gives rise to a higher value though. The average distance between the Kiessig fringes of 0.056 nm^{-1} hints at a film thickness of 113 nm,[94] and indeed, fitting of the scan for the mesoporous film in Figure S20D (Supporting Information) yields a thickness of 98 nm. In addition, the porosity of the thin film can be determined based on the critical wave vector q_c originating from the difference in electron density at the air/IrO_2 interface.[95–97] While a non-templated IrO_2 thin film (Figure S20D, Supporting Information) leads to $q_c = 0.618$ nm^{-1} (corresponding to a density of 6.70 g cm^{-3}), the introduction of mesopores into the IrO_2 phase lowers the average electron density, causing a reduction in q_c.[96,98,99] If a sufficiently high porosity is present so that the electron density of the thin film comes below that of the silicon substrate, the mesoporous film becomes a waveguide, and two critical wave vectors are observed: one of the thin film (here: $q_c = 0.244$ nm^{-1}) and one of the substrate (here: $q_c = 0.315$ nm^{-1}).[96,100] From the thin film's q_c, an electron density of 420 nm^{-3} can be determined (see Supporting Information for more details), which corresponds to a porosity of 84% when compared with the electron density of crystalline tetragonal IrO_2 (2700 nm^{-3}). Alternatively, the density obtained from fitting the experimental XRR curve (1.55 g cm^{-3}) can be related to the density of the non-templated sample, yielding a porosity of 77%, which should be more reasonable due to the low crystallinity of IrO_2 synthesized here. Compared to this evaluation, the refractive index of the mesoporous thin film ($n = 1.68$) measured with ellipsometry delivers a porosity of 55% when compared with crystalline IrO_2 ($n = 2.50$)[101] according to the Bruggemann effective medium approximation[102,103] (BEMA). This deviation evokes the assumption that this ellipsometry evaluation model becomes inaccurate for mesoporous samples, in particular, as the film thickness determined by XRR (9.9 nm) and ellipsometry (11.7 nm) are in good agreement in the case of the non-templated sample. In the case of the mesoporous sample, evaluation of the XRR data becomes more challenging because of the superposition of the reflectivity curve with Bragg peaks originating from the ordered array of mesopores. The spherical pores, which are compressed along the film normal, possessing an ellipsoidal shape,[20,28,102] are stacked layer-wise with a defined pore wall between each pore layer, causing periodically appearing Bragg peaks.[96,99,104] Their position q gives access to the layer period (pore-to-pore distance) being equal to $2\,\pi\,i\,q^{-1}$ if their order i is known. In the case of the curve of the mesoporous film in Figure S20D (Supporting Information), a broad background at ≈0.35 nm^{-1} can be observed, leading to a deviation between the simulated and experimental reflectivity curve. Assuming a second order Bragg peak (the first order one would be hidden in the specular region below q_c), a layer period of 36 nm is obtained, which matches very well the lateral pore-to-pore distance found in the mesoporous carbon film (see SEM cross-section in Figure 11A below) being composed of a pore height of 20 – 25 nm and a 10 nm thick wall. Thus, the mesoporous IrO_2 thin film seems to be a suitable comparison sample for the carbon-based one in terms of pore morphology.

The transport perpendicular through the thin film (including substrate) was determined using electrochemical impedance spectroscopy (EIS) after mounting the thin films into a metal screw clamp, as sketched in **Figure 10**C and exemplified in the photos in Figure S21 (Supporting Information). Within an internal comparison, the aforementioned mesoporous carbon and mesoporous IrO_2 thin films (both deposited on polished titanium plates) were contrasted to a blank, polished titanium plate (conductor) and a silicon wafer (semiconductor) as border cases on a conductivity scale. It is important to mention that only effective

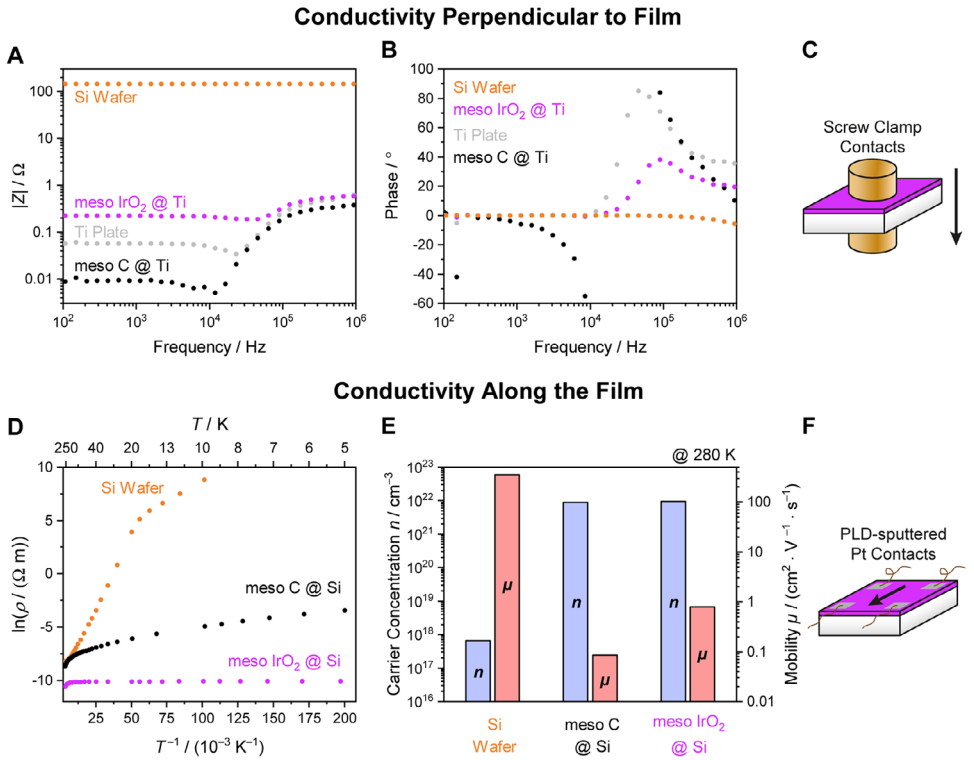

Figure 10. A,B) Bode plot of the impedance spectra of a silicon wafer (orange), a titanium substrate (gray), and a mesoporous hard carbon (black) and IrO_2 thin film (violet) deposited on titanium, recorded at room temperature in transversal direction as shown in C) the sketch of an exemplary sample. D) Arrhenius plot of the resistivity of mesoporous carbon and IrO_2 thin films deposited on silicon wafers, and E) the corresponding charge carrier concentration (blue) and mobility (red) at 280 K determined by a Hall measurement in van-der-Pauw geometry, as illustrated in F) the scheme of a thin film.

impedances and conductivities are measured for the mesoporous samples here and not the material-specific values of the solid skeleton material (i.e., pure carbon and pure IrO_2) as porosity decreases the effective conductivity compared to a non-porous sample.[105] Yet, due to the similar morphology of both samples, the internal comparison based on the effective values is sufficient.

At high frequencies, the impedance spectrum of the silicon wafer is governed by capacitive contributions, which can be seen by the negative phase in the Bode plot (Figure 10B) and negative imaginary values in the Nyquist plot (Figure S22D, Supporting Information). Contrarily, the impedance of the metal-based samples is dominated by inductive contributions in the high frequency region (arising probably from the setup) leading to a positive phase (Figure 10B) in the Bode plot and positive imaginary parts in the Nyquist plot (Figure S22, Supporting Information). However, with decreasing frequency, this inductive contribution diminishes, and the properties of the thin films control the impedance. At low frequencies, the phase of all samples approaches zero so that the impedance is fully governed by its real part, i.e., an ohmic resistance. Therefore, the absolute value of the impedance measured at low frequencies in Figure 10A corresponds to the resistance of the entire sample (thin film and substrate) in transversal direction following the trend: mesoporous carbon (9 mΩ) < Ti (56 mΩ) < mesoporous IrO_2 (215 mΩ) << Si (145 Ω). These values demonstrate that a model electrode made from a mesoporous hard carbon thin film deposited on a titanium plate possesses a similarly low resistance, i.e., high electric conductivity, as an IrO_2-based model electrode applicable for electrocatalysis. It should be noted that the measured resistance value of the highly conductive samples (such as the metal-based samples) is affected by large uncertainties due to a contact resistance contribution. As the pressure for the screw contacts clamping the samples could not be controlled in a defined way, even small variations in the contact resistance between electrodes and sample may dominate the overall impedance at low frequencies. Thus, the results for the samples with a resistance below roughly 1 Ω are less reliable than those for silicon wafer with a significantly higher resistance. This explains why the mesoporous carbon sample features surprisingly a lower resistance than the parent metal plate expected to yield the highest conductivity. The same holds true for the IrO_2 sample, which is expected to be more conductive than non-graphitic carbon,[87,106] although the formation of a thin less conductive TiO_2 layer on the backside of the substrate during calcination in air might also be responsible for a lower overall conductivity of the IrO_2 sample. Nevertheless, a low resistance in both the carbon and IrO_2 sample can be concluded from this experiment, whose reliability is supported by the temperature-dependent impedance measurements (Figure S23A, Supporting Information) of a mesoporous carbon thin film on silicon (this substrate was used to increase reliability of the obtained resistance). The Arrhenius plot of the measured resistance (Figure S23B, Supporting Information) shows a change in the dominant transport mechanism at 263 K, at which

the activation energy increases from 12.4 meV (low temperatures) to 26.2 meV (high temperatures). This behavior is reported for other thin films on silicon and can be explained with a release of charge carriers trapped at the Si/coating interface upon exceeding a threshold temperature.[107] This confirms that indeed the transport through thin film and substrate was measured with the screw clamp setup.

An unambiguous comparison between solely non-graphitic carbon and IrO_2 with regard to their electric transport properties requires an in-plane conductivity measurement, i.e., along the mesoporous thin film. For this reason, the substrate, the mesoporous carbon sample, and the IrO_2 counterpart were sputtered with platinum in all four corners using pulsed-laser deposition and contacted with conducting silver and copper wires each prior to performing transport measurements in van-der-Pauw geometry as shown in the sketched sample in Figure 10F and the photos in Figure S21 (Supporting Information). Silicon was used as substrate due to its comparably high electric resistivity, which ensures that the measured transport properties are dominated by the properties of the deposited thin film layer. The temperature-dependent resistance measurement of the Si substrate (without external magnetic field) yields the transport behavior expected for n-doped silicon (orange data in Figure 10D; determined values in Figure S23C, Supporting Information):[108–110] At low temperatures (<20 K), conduction follows a tunneling-controlled hopping mechanism between the donor states with a very low activation barrier (6.5 meV). With increasing temperatures, the donor-based charge carriers are consecutively thermally activated with an activation energy of $E_A = 23.9$ meV (corresponding to a dopant energy level of $E_D = 2\ E_A = 47.8$ meV[108] and being in good alignment with 46 meV as expected for phosphorus[111] as dopant). Finally, at high temperatures (>100 K), a plateau is found originating from the saturation of the carrier concentration when all donor-based charge carriers are thermally activated from the donor into the conduction band. The fact that the sheet resistance R of the mesoporous samples (Figure S23C, Supporting Information) neither coincides with the resistance of the silicon substrate nor shows a comparable temperature behavior confirms that the measured resistance is dominated by the mesoporous thin film, i.e., the transport indeed occurs in the thin film, and a contribution from the substrate can be neglected. When multiplying the sheet resistance by the thickness of the layer in which the transport occurs (Si: 450 µm, carbon: 300 nm, and IrO_2: 50 nm), the corresponding (thickness-independent) resistivity ρ can be estimated. The Arrhenius plot of ρ in Figure 10D shows that the mesoporous IrO_2 film has one order of magnitude higher in-plane conductivity than the mesoporous hard carbon film (at 280 K, $\rho = 2.37 \times 10^{-5}$ Ω m and $\rho = 1.67 \times 10^{-4}$ Ω m, respectively) in contrast to the transversal measurement. The general temperature dependency reveals a transport behavior in both thin films with a pronounced hopping regime (plateau) at low temperatures followed by a steep decrease with increasing T being characteristic for highly doped semiconductors.[112] In the case of mesoporous carbon, the slope in the low temperature region is higher than in case of mesoporous IrO_2, which hints at a very broad impurity band.[108] This is reasonable as there are various possible defects (acting as dopants) in non-graphitic carbon[67] (leading to the pronounced D band in Figure 5C), probably higher in concentration and with less-defined energy levels than in the metal oxide[87,90] (e.g., oxygen vacancies).

When applying an external magnetic field, the charge carrier concentration n and their mobility μ can be determined by Hall measurements (Figure 10E). The values determined for the silicon substrate are in excellent agreement with values reported for phosphorus-doped silicon[113] and confirm the overall reliability of this method. In case of the mesoporous samples, a comparable charge carrier density n is observed for mesoporous IrO_2 (9.36×10^{21} cm^{-3}) and mesoporous hard carbon (8.79×10^{21} cm^{-3}) at 280 K but a noticeably higher resistivity is measured in case of mesoporous carbon. This discrepancy in resistivity between the carbon- and IrO_2-based samples in Figure 10D indicates a lower mobility of the charge carriers in the mesoporous carbon compared to IrO_2 (0.086 vs. 0.787 cm^2 V^{-1} s^{-1}). Although the carrier densities appear to be very high, both n and μ of the IrO_2 sample are in very good alignment with results reported by Sachse et al.[87] for mesoporous IrO_2 thin films. From all these experiments, it can be concluded that mesoporous carbon itself shows a slightly lower conductivity than the comparative IrO_2 model system, but can compete with the latter when regarding the entire model electrode, including the metal substrate.

2.5.2. Electrochemical Stability

The stability of the mesoporous carbon is of crucial importance for electrocatalysis if used as a catalyst support. Although the carbon support would be protected from the electrolyte by the actual catalyst (e.g., a thin layer of IrO_2) in real electrocatalysis, direct exposure to the acidic electrolyte while applying an oxidizing potential acts as a stress test to study the stability of the non-graphitic carbon. Therefore, a mesoporous carbon thin film on titanium was built in an electrochemical flow cell made from poly(ether ether ketone) (PEEK), contacted from the backside with a stainless steel plate, and flushed with 0.5 M sulfuric acid (flow rate of 2 mL min^{-1}) as sketched in **Figure 11D**. As a stability protocol, a long-term cyclovoltammetry (CV) within a (OER-active) potential regime of 1.45 and 1.60 V (vs. SHE) was adapted from Duran et al., who studied the stability of porous IrO_2 in acidic water splitting.[114] The evolution of the current density together with SEM images of the pore system after different polarization times give insight into the electrochemical stability of the porous system. Here, two analogous carbon thin films were analyzed: one for a short-term polarization (75 min) and one for a long-term measurement for 24 h.

Before exposing the film to the harsh OER conditions, an ordered mesoporous structure with spherical pores of 69 nm in diameter can be observed by SEM at the surface (Figure 11E) and throughout the entire film (film thickness of 370 nm) when analyzing the cross-section of an analogous carbon reference film on silicon (Figure 11A). On a macroscopic level, the carbon film appears homogeneously black, as shown in the photo in Figure 11B. If this film experiences a linearly swept anodic potential under acidic conditions, a small periodically oscillating current density of a few µA cm^{-2} can be recorded (Figure 11J; Figure S24, Supporting Information). This current is expected to originate mainly from the carbon corrosion reaction (CCR) shown in

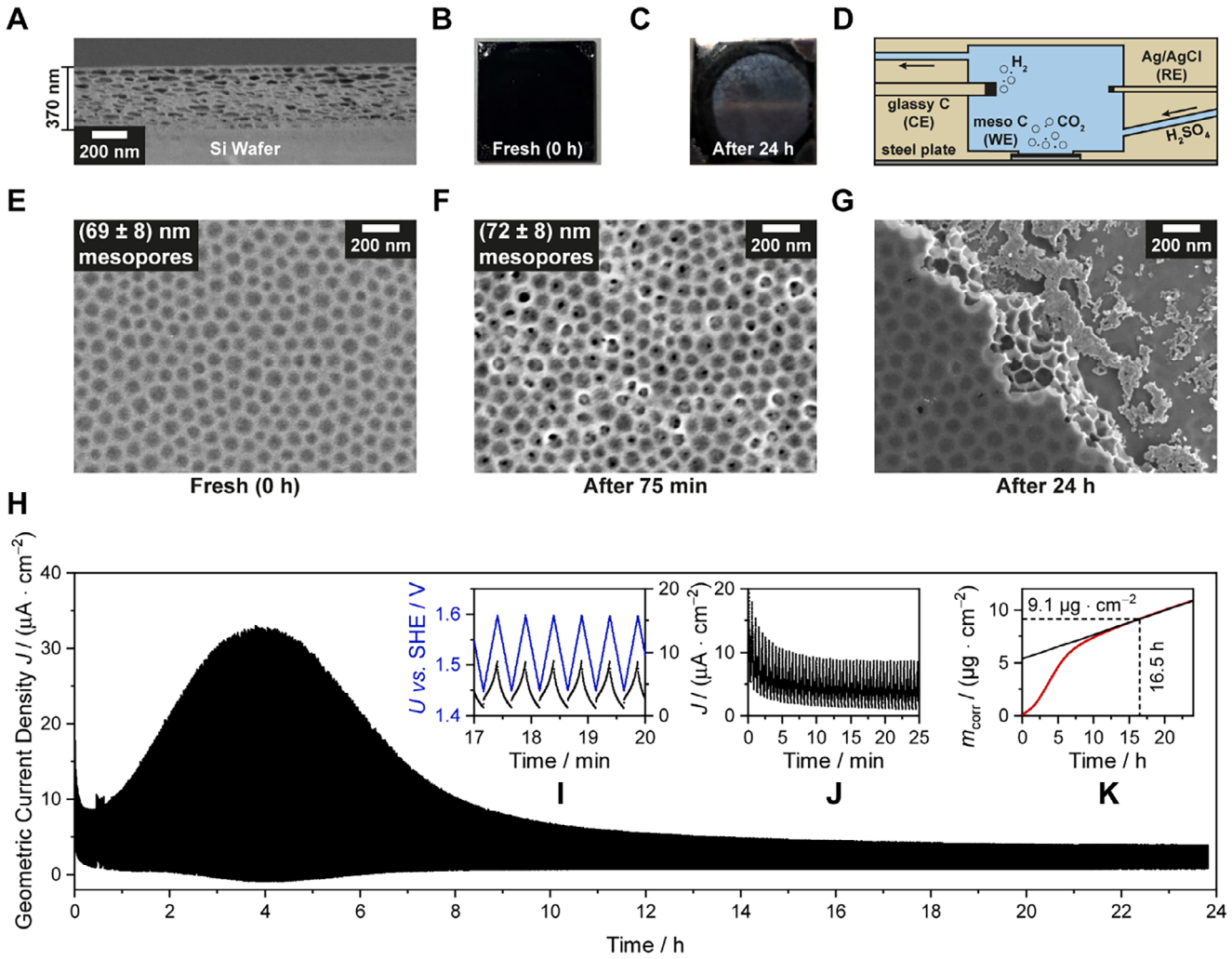

Figure 11. SEM images of A) the cross-section and E) top-view of a pristine mesoporous carbon thin film on titanium and F) one after 75 min and G) after 24 h of cyclic polarization between 1.45 and 1.60 V against SHE in D) an electrochemical flow cell. Photos of B) the fresh film before and C) after 24 h of polarization are displayed together with H) the monitored geometric current density. The insets show the evolution of the current density (black) in a I) 3 min and J) 25 min time interval upon applying a cycled linear potential (blue) recorded with 0.01 V s^{-1} as well as K) the mass of corroded carbon (red) after integration of the current density and conversion following the Faradaic law under the assumption of pure carbon corrosion without side reactions.

Equation 1, which was confirmed to be the dominating reaction starting from 1.4 V vs. SHE for different carbon materials according to differential electrochemical mass spectrometry (DEMS).[57,58,115] The contribution of the OER only becomes significant above 1.6 V vs. SHE in the case of carbon.[115]

$$C + 2H_2O \rightarrow CO_2 + 4H^+ + 4e^- \quad (1)$$

The evolution of the current density shows an initial decay before reaching a state of constant current (between 20 and 75 min in Figure S24D, Supporting Information). This initial decrease can be explained by the establishment of a stable concentration profile of the reactants and products near the electrode surface, as typically observed in chronoamperometry and described by the Cotrell equation.[116] Such a trend is slightly discernible in the studies on porous IrO_2 with the analogue cycling protocol as well.[114] After polarization for 75 min (150 CV cycles), no significant morphological changes occur. The SEM image in Figure 11F reveals a pore size being slightly larger (72 nm), possibly due to a minimal enlargement upon consecutive carbon corrosion, but the deviation is not significant if the polydispersity of the pore size is considered. Additionally, the CV scans between 0.2 and 1.7 V vs. SHE before and after polarization (Figure S24C, Supporting Information) of the mesoporous carbon film are almost identical featuring a small reductive current and a larger oxidative current at the borders, which can be assigned to the HER and CCR, respectively.[57,58] Hence, no severe change in carbon occurred. Yet, the pore structure in the SEM image in Figure 11F appears slightly better connected as more pore necks of the sub-surficial pores can be observed compared to the initial state (Figure 11E).

When performing a long-term cycling on a second sample, a different evolution in current density is found (Figure 11H): Initially, the current density shows the trend discussed before

(Figure 11J). However, after the region of constant current density, J starts to increase after 1 h and reaches a maximum at 4 h prior to decreasing until a constant region is established again after 14 h of polarization. Assuming a proceeding carbon corrosion, this behavior can be explained by an opening of the formerly (rather) isolated mesopores (see Figure 7) by electrochemical etching, which results in an increase in exposed/accessible surface area, leading to an increase in corrosion current density. While the CCR continues, non-graphitic carbon material is consecutively degraded, which results in a decrease in surface area after a certain point. Thus, an apex followed by a decrease in J is found until no carbon is present anymore. Regarding the macroscopic appearance of the sample (shiny circle in Figure 11C) as well as the mesoscopic morphology at the border between carbon being exposed and not exposed to the electrochemical cell by SEM (Figure 11G) after 24 h of polarization (2900 cycles), a complete degradation of the mesoporous thin film can be clearly confirmed. The final region of constant J after 14 h is then most likely a consequence of the uniform leaching of the substrate. Understandably, the CV scans of the sample before and after 24 h of polarization do not coincide anymore, as the carbon layer is removed completely (Figure S24A, Supporting Information). Assuming that only the CCR as a four-electron process takes place as expected from DEMS studies,[57,58] the current density in Figure 11H can be integrated to obtain the transferred charge Q and converted to the mass of corroded carbon m_{corr} as a function of reaction time following Faraday's law (red curve in Figure 11K). After 16.5 h, the sigmoidal growth curve merges into a linear behavior (which can be assigned to substrate corrosion). These data imply that the overall amount of 9 µg cm^{-2} of mesoporous carbon is fully corroded after ≈16.5 h.

Overall, this study demonstrates that the mesoporous non-graphitic carbon itself is not long-term stable under OER conditions. Still, a remarkably long time is needed to significantly corrode the carbon material, especially considering the large surface area of this porous system (see Figure 6D) and the CCR that is expected to occur already at 207 mV vs. SHE[58] according to thermodynamics. Furthermore, the carbon is protected by a layer of the actual catalyst in electrocatalysis and thus is not in contact with the electrolyte needed to decompose the carbon support. Even if a few small uncoated spots of the support should be exposed to the electrolyte, severe corrosion would require a long time due to the small exposed area, and the catalytic activity should not be significantly reduced as long as electric conduction over the pore wall is still ensured. Indeed, recent studies of carbon hybrid materials for electrocatalysis confirm a promising stability in both acidic[117] and alkaline[118] water electrolysis. Therefore, the mesoporous carbon in this study remains a promising support for electrocatalysis with regard to stability.

2.5.3. Accessibility of the Pore System

Concerning the last prerequisite, i.e., the accessibility, the mesoporous carbon thin films (both before and after 75 min of corrosion) were infiltrated with a tracing electrolyte, and the spatial ion distribution within the mesoporous system was monitored in 3D by SIMS. Similar to previous studies on metal oxide thin films,[51,119] the appearance of tracing ions deep inside the thin film acts as marker for an interconnected and accessible pore system. By that, the mutual accessibility of the fresh film can be checked as well as a possible increase in accessibility upon brief carbon corrosion. In this study, however, cobalt nitrate could not be used as tracing electrolyte (in contrast to the previous studies) as the carbon film shows only appropriate ion counts in negative ion mode while Co^{2+} ions need to be measured in positive ion mode. Thus, an easily detectable, soluble, stable, and unambiguous (that means an ion that can only be assigned to the added salt) anion probe is required. Therefore, lithium tetrafluoroborate ($LiBF_4$) was used instead. Using SIMS, the depth profiles were recorded, and the evolution of the carbon-based (here, following a small and a heavy carbon fragment) and TiC-based (C_2^- and TiC_2^-) signals was investigated, similar to the measurements in Figure 8 but extended by the $Li_2F_3^-$ and BF_4^- signals of the tracing electrolyte. As shown in **Figure 12A** for the fresh carbon film before carbon corrosion, the $LiBF_4$-derived fragments can be found within the hard carbon thin film but their signals do not show a congruent trend to the carbon-based signals. This implies that the tracer penetrated the carbon film roughly up to the top 20 – 30% but was not capable of fully accessing the entire mesoporous coating. In this qualitative study, no further AFM experiments were carried out, and, hence, the signal evolution is plotted against the fluence of ions sputtering the surface instead of the actual depth. This becomes more apparent from the 3D overlay in Figure 12B, confirming the surficial infiltration of the carbon film by $LiBF_4$. As a result, the fresh hard carbon thin film possesses only low accessibility.

However, after 75 min of electrochemical corrosion, the mesoporous carbon samples yield a different result. In this case, the $Li_2F_3^-$ profile in Figure 12D evolves in parallel to the carbon-derived fragments. The intensity fluctuations of the mass signals close to the surface (decay and increase of $Li_2F_3^-$ signal intensity, local maximum of BF_4^- signal intensity, and initial increase in carbon signal intensity between a fluence of 0 and 2×10^{16} cm^{-2}) most likely originate from the precipitation of residual lithium salts, fluorides, and BF_4-containg species at the surface of the thin film as confirmed by the surface images in Figure S25 (Supporting Information). Nevertheless, the high intensity of the $LiBF_4$-derived signals until the carbon/TiC interface demonstrates a complete infiltration of the mesoporous carbon, which is further supported by the 3D overlay in Figure 12C. This experiment also confirms the previous assumption of an increase in pore accessibility upon electrochemical corrosion, presumed on the basis of SEM and the evolution of the corrosion current density in Figure 11. Consequently, the initially poor accessibility of the mesoporous hard carbon thin film can be overcome by applying a short electrochemical etching to widen the pore throats. The accessibility thus obtained is mandatory for application to ensure an even coating (e.g., by atomic layer deposition) or catalysis without diffusion limitation. Yet, even without etching, the pristine mesoporous carbon with isolated pores is still promising for other applications, such as sodium-ion batteries, in which isolated mesopores proved to be beneficial.[52]

In summary, ordered mesoporous hard carbon thin films on titanium possessing spherical pores with 70 nm in diameter showed to be electrically conductive, sufficiently stable under acidic and oxidizing conditions, and accessible for probe

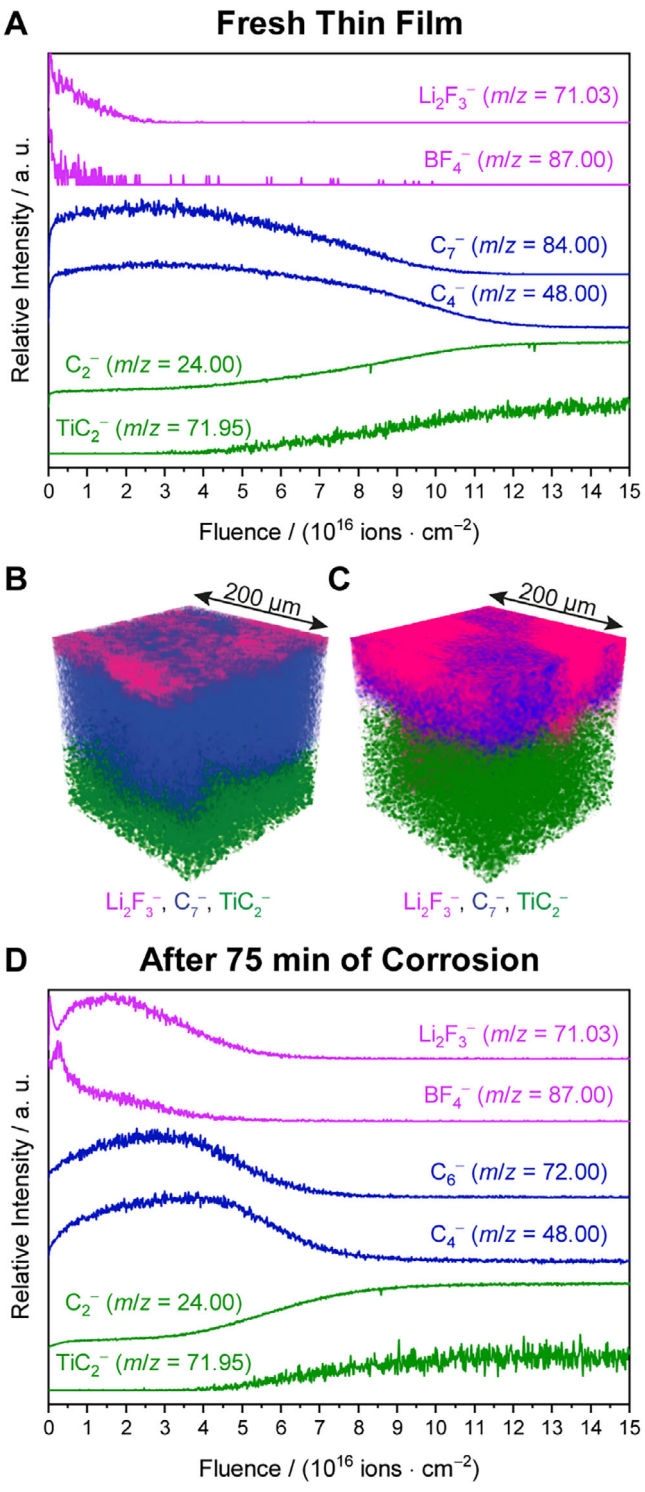

Figure 12. Accessibility of mesoporous carbon thin films. SIMS depth profiles of A) a fresh and D) a briefly electrochemically corroded mesoporous carbon thin film on titanium infiltrated with a $LiBF_4$ tracing electrolyte comprising the evolution of the ion signals assigned to the $LiBF_4$ phase in violet, the hard carbon phase in blue, and the TiC phase in green as well as the 3D overlay of the $Li_2F_3^-$, C_7^-, and TiC_2^- signal of the B) fresh and C) briefly corroded sample after infiltration.

molecules after brief electrochemical corrosion, rendering them a promising support for electrocatalytic applications.

3. Conclusion

Having experienced Helmut Cölfen as a colleague for many years, we are grateful for his courage to bring a seemingly naïve question onto the stage of materials science, namely, how simple inorganic crystalline substances are formed from molecular entities and how the crystallization can be manipulated. In particular, his passion in emphasizing the necessity for understanding the nature and relevance of the amorphous state in nucleation and crystallization was an important momentum for us to elucidate the transition of amorphous carbon into graphene-like materials. As an important part of our study, we addressed the important question of the fate and role of block copolymers in the carbonization process, which we would certainly have ignored if one of the authors (B.S.) had not been exposed to Helmut Cölfen's work for several years. The fact that organic additives – even in small amounts – may affect the nucleation and crystallization of classic inorganic salts, was put forward by Helmut and represents a relevant question in our studies on carbon, too.

This study thus aimed at the preparation and deep characterization of mesoporous carbon thin films with high electric conductivity on metallic substrates, which are suitable for electrochemical applications. While we confirmed an ordered mesoporous structures (with 70 nm mesopores) with the aid of gas physisorption and electron microscopy, we elucidated the formation and sp^2-based microstructure of the non-graphitic carbon by TG-MS, XRD, Raman spectroscopy, and TEM images. Employing ToF-SIMS, GIXRD, and SEM, we observed an unexpected and severe substrate corrosion leading to a significant incorporation of TiO_2 into the carbon material when carbonized in pure argon. A mixture of 85 vol.% argon and 15 vol.% CO showed to be mandatory to avoid substrate oxidation yielding a homogeneous mesoporous carbon film separated from the substrate by a thin carbide interphase. XPS and XRD experiments confirmed that CO influences neither the carbon microstructure nor composition.

The corrosion-free carbon thin films were tested for their suitability as model supports for electrocatalysis in terms of electric conductivity, stability, and accessibility. Regarding electric transport, the carbon thin film demonstrated to be able to compete with analogously porous IrO_2 model electrodes as shown by impedance and Hall measurements. The initial poor accessibility of the carbon thin film (deduced from SIMS depth profiling after infiltration with a tracing solution) was successfully overcome by short-term polarization under (acidic and oxidizing) OER conditions, under which the carbon samples generally revealed a surprisingly high stability even in an uncoated (i.e., unprotected) state.

These properties render the mesoporous carbon thin film a promising support for electrocatalysis (e.g., in water splitting), on which a catalytically active material (such as IrO_2) can be deposited as atomically thin layers to reduce the overall loading of active yet precious materials. In the future, two questions need to be addressed: On the one hand, if a metal oxide like IrO_2 can be deposited as a homogenous layer onto carbon at all, and on

the other hand, if the resulting electrocatalyst can keep up with pure IrO_2 catalysts in terms of activity and stability. Beyond this application, the presented work acts as a general, extensive guideline for characterizing non-graphitic carbon thin films, which can be used for several systematic studies in electrochemistry (e.g., sodium-ion batteries) due to their well-defined structure.

The presented work benefited from Helmut Cölfen also in regards how to perform studies involving self-assembled materials and complex analytics: First, one should be courageous to ask basic questions, especially when it comes to crystallization. Second, collaboration in cutting-edge analytics, especially in such demanding fields as self-assembled materials, works best on the basis of a friendly partnership and respectful cooperation. Thus, our complex analytical studies would not have been possible without such unselfish collaboration of many co-workers, which also was one of the outstanding character traits Helmut was known for and by which he certainly had a significant impact on many colleagues and students, who had the pleasure to work with him.

4. Experimental Section

Synthesis of the Soft Template: The PEO-*b*-PHA block copolymer was prepared by a two-step procedure analogous to the previous study[51] and based on the initial report of Lokupitiya et al.[50] α-Methyl-ω-hydroxy poly(ethylene oxide) (PEO-OH) with an average molecular weight of 20 kDa (as provided by the supplier) was purchased from Sigma-Aldrich. According to ^{1}H-NMR end group analysis (Figure S1A, Supporting Information), the number-weighted molecular weight (M_n) of PEO-OH amounts to 16.6 kDa (372 EO units) with a polydispersity index of 1.03 based on gel permeability chromatography (Figure S1B, Supporting Information). Experimental details on the Steglich esterification yielding the macroinitiator PEO-Br and subsequent supplemental activator reducing agent radical atom transfer polymerization (SARA ATRP) can be found in the last article,[51] while only a brief description is given here.

For macroinitiator synthesis, 4.000 g (0.20 mmol, 1.0 eq) poly(ethylene oxide) methyl ether (PEO-OH, 20 kDa, Sigma Aldrich) were dissolved in 10 mL anhydrous dichloromethane (DCM, 99.8%, Acros Organics) under argon in a 50 mL round bottom flask by stirring at room temperature. After adding 22 µL (0.24 mmol, 1.2 eq) 2-bromopropionic acid (99%, Acros Organics), 10 mg (0.08 mmol, 0.4 eq) 4-dimethylaminopyridine (DMAP, ≥ 99%, Sigma Aldrich), and 95 mg (0.46 mmol, 2.3 eq) *N*,*N*′-dicyclohexylcarbodiimide (DCC, 99%, Sigma Aldrich) to the colorless solution, it was stirred for 20 h at room temperature under argon atmosphere. Excess DCC was quenched with 5 µL of a 1 M hydrochloric acid (Grüssing GmbH), and the turbid reaction mixture was diluted with 50 mL DCM, filtered, and concentrated under reduced pressure. The colorless residue was dissolved in 10 mL tetrahydrofuran (THF, technical grade, Thermo Scientific) and precipitated twice in 250 mL cold diethyl ether. Drying in a vacuum oven at 40 °C for 18 h resulted in 3.552 g (0.18 mmol, 88%) of a colorless powder.

The PEO-*b*-PHA block copolymer was synthesized by a supplemental activator reducing agent atom transfer radical polymerization (SARA ATRP) with a pretreated[120,121] copper wire wrapped around the stirring bar as reducing agent. In a 100 mL Schlenk round bottom flask, 1.000 g (0.05 mmol, 1.0 eq) PEO-Br, 44 mg (0.15 mmol, 3.0 eq) tris(2-pyridylmethyl)amine (TPMA, >98.0%, TCI CO.), 11 mg (0.05 mmol, 1.0 eq) $CuBr_2$ (>99%, water free, Acros Organics), and 2.4 mL (13.64 mmol, 274 eq) hexyl acrylate (98%, Sigma Aldrich) were dissolved in 3.2 mL anhydrous *N*,*N*-dimethylformamide (DMF, 99.8%, Acros Organics) and stirred at 70 °C for 16 h under argon atmosphere. The dark orange gel was dissolved in 80 mL THF, passed over a column of basic alumina, concentrated under reduced pressure, and precipitated twice in 200 mL cold methanol (cooled with an ethyl acetate/liquid nitrogen freezing mixture). The fine colorless precipitation was recovered by filtration over a Büchner funnel and transferred to a Petri dish prior to drying in a vacuum oven at 40 °C for 15 h leading to 1.698 g of a yellow gel. The PHA's degree of polymerization was determined to be 180 (PEO_{372}-*b*-PHA_{180}) according to ^{1}H-NMR in $CDCl_3$ (Figure S1C, Supporting Information) while the polydispersity index amounts to 1.55 according to gel permeability chromatography (Figure S1D, Supporting Information). Note that both the apparent number-weighted molecular weight of 60.2 kDa and the polydispersity from GPC are overestimated due to residual PEO-Br macroinitiator, which, however, does not interfere with the soft templating process.[51]

Synthesis of Mesoporous Carbon Powders: In a 4 mL glass vial, 190 mg of the soft template were dissolved in 2.9 mL absolute ethanol (99.8%, Fisher Chemicals) by sonication for 40 min at 40 °C and 37 kHz. In a second vial, 330 mg resorcinol (99%, Sigma Aldrich) were dissolved in 870 µL deionized water upon stirring at room temperature for 20 min. After adding 30 µL of a 5 M hydrochloric acid (made from 583 µL water and 417 µL fuming hydrochloric acid purchased from Fluka) to the carbon precursor, the polymer solution was added as well followed by the addition of 275 µL triethyl orthoacetate (97%, Thermo Scientific) and 330 µL of a 37 wt.% aqueous formaldehyde solution (10 – 15% methanol as stabilizer, Sigma Aldrich) after brief stirring. The reaction mixture was stirred for 60 min at 40 °C prior to casting into a Petri dish. The slightly orange solution was dried at 80 °C in a drying oven, yielding an intensely orange brittle residue. The latter was scratched off and transferred to a crucible. After carbonization in a muffle furnace in nitrogen atmosphere (3 h at 400 °C, 3 h at 800 °C, 1 K min^{-1} heating rate each) together with a second crucible filled with ≈200 mg copper powder (99%, Acros Organics) as sacrificial reducing agent and grinding, 125 mg of a black powder were obtained.

In case of the non-templated powder (referred to as dense reference), the same protocol was applied replacing, however, the polymer solution by the same volume of pure absolute ethanol.

Preparation of Mesoporous Carbon Thin Films: Prior to spin coating, the titanium plates (10 mm x 10 mm, 1 mm thickness, 99.2%, Evek GmbH) were deburred with P400 silicon carbide paper and polished to a mirror finish with an *AutoMet 300* polishing machine by *Buehler* using polycrystalline colloidal diamond suspensions of consecutively decreasing size. The detailed protocol comprises in-phase polishing with 260 and 130 rpm (rotation rate of lower and upper rotor, respectively) with 15, 1, and 0.05 µm diamond colloids for 30, 20, and 10 min, respectively, and an applied force of 15, 15, and 10 N to press the titanium plates against the lower rotor. Following polishing, the substrates were cleaned by ultrasonication in acetone (to remove residual wax used to attach the substrates to the polishing machine), water, ethanol, and acetone for 10 min at 37 kHz each. Before use, all substrates were further cleaned in a UV ozone cleaner (*Ossila*) for 10 min.

Regarding spin coating, the same reaction mixture was used as for the preparation of mesoporous powders. Yet, instead of casting into a Petri dish, the solution was sonicated at 37 kHz for 5 min and used for spin coating with a *SCC-200* spin coater from *KLM*. Here, 30 drops (≈250 µL) were dropped within 60 s with a Pasteur pipette on the polished Ti plates rotating with 15 rps. After further 2 min of rotation, the films were transferred to a pre-heated furnace for drying, in which they were kept for 12 h at 80 °C. Carbonization was performed in a tube furnace (*Nabertherm*) in a mixture of flowing argon (85 mL min^{-1}) and carbon monoxide (15 mL min^{-1}) using the same heating ramp applied for the powders.

Preparation of Mesoporous IrO_2 Thin Films: Reference samples of mesoporous IrO_2 thin films on polished titanium plates and silicon wafers, respectively, were prepared by spin coating. First, 15 mg of the PEO-*b*-PHA soft template were dissolved in a mixture of 500 µL of DMF (technical grade) and 100 µL of THF (technical grade) by sonication at 37 kHz and 40 °C for 30 min (the vessel was sealed with a tap and Parafilm to avoid solvent evaporation). In the case of the non-templated sample, the pure solvent mixture was used instead. Thereafter, 20 mg of $IrCl_4 \cdot 2H_2O$ (99.9%, 52% Ir, abcr) were dissolved in a mixture of 500 µL of absolute ethanol and 100 µL of hydrochloric acid (fuming, ≥37%, Fluka) by stirring at room temperature for a few minutes. The polymer solution was added dropwise to the precursor solution with a glass pipette within 5 s, and the resulting deep purple solution was stirred for a further 2 min. Upon spin coating,

50 µL of the reaction solution was deposited on the respective substrate (cleaned in a UV ozone cleaner for 10 min before coating) rotating with 15 rps. After 2 min of rotation with 15 rps, the samples were rotated with 50 rps for 1 s to remove excess precursor solution before transferring to an oven pre-heated to 90 °C. After drying at this temperature for 2 h, the thin film were calcined at 130 °C for 1 h and 350 °C for 6 h (heating rate: 0.13 and 0.61 K min^{-1}).

Characterization Techniques: Proton-nuclear magnetic resonance (^{1}H NMR) spectra were measured using an *Avance II 400 MHz HD* by *Bruker* in $CDCl_3$ at 25 °C. All spectra were evaluated with *MestReNova 14.1.2* and referenced to the solvent peak at $\delta = 7.26$ ppm. Gel permeability chromatography (GPC) of the macroinitiator and the block copolymer was executed with tetrahydrofuran as eluent at room temperature and with a flow rate of 0.5 mL min^{-1}. The instrument was equipped with a UV (*TSP UV 1000*) and a simultaneous differential refractive index detector (*Shodex RI-101*) as well as a 300 mm x 8 mm *PSS SDV linear M* column packed with 3 µm particles (10^2–10^6 Da molar mass regime). The polymer solution samples (circa 0.15 wt.% polymer in THF) were filtered through a 0.45 µm filter before 100 µL were injected. Calibration was performed with poly(styrene) standards purchased from *PSS* (Mainz, Germany). Thermogravimetric studies coupled with mass spectrometry (TG-MS) were carried out in argon using a *STA40PC thermoscale* provided by *Netzsch* (resolution of 2 µg and thus $\Delta m_{rel} = 0.01\%$) within a temperature range from 30 to 1000 °C with a heating ramp of 5 K min^{-1} and the heating ramp used for the carbon synthesis, respectively. Meanwhile, a mass spectrum covering an m/z interval between 12 and 100 was recorded constantly with the aid of a *QMG451* quadrupole mass spectrometer by *Balzers*. Raman spectra were acquired at room temperature with a *Renishaw inVia* Raman microscope in backscattering geometry using an excitation wavelength of 633 nm and 515 nm, respectively. Spectra were recorded with a charge-couple device (CCD) detector in a spectral range of 100–3200 cm^{-1} with a step size of 2 cm^{-1}, integrating five scans of 10 s exposure time each. Powder X-ray diffraction (XRD) of the carbon powders was performed with a *PANalytical Empyrean Series 2* diffractometer in Bragg-Bretano geometry under ambient conditions in a 2θ range of 5 to 115° with monochromatized Cu Kα radiation ($\lambda = 1.5406$ Å, a Ni filter for suppression of Cu Kβ radiation). The optics consisted of 1° anti-scatter slits, a 0.5° divergence slit, and 0.04 rad sollar slits. XRD data were exported with *HighScore Plus* and analyzed with an algorithm based on Ruland and Smarsly[74] implemented in the *OctCarb* script[75] in *GNU Octave*.[76] Scanning electron microscopy (SEM) images were obtained with a *Zeiss GeminiSEM 560* microscope using an *InLens* detector, a working distance of 2.5 mm, and an acceleration voltage of 1 kV. To enhance the conductivity, samples were coated with platinum using a *Leica EM ACE600* sputter coater. In the case of cross-sectional imaging, the samples were contacted with conducting silver varnish before sputtering. All images were evaluated with the *Fiji ImageJ* software. Nitrogen physisorption isotherms were recorded at 77 K on an *Autosorb iQ* by *Quantachrome Instruments* (Boynton Beach, USA, FL). The data were analyzed with the *ASiQwin* software applying a quenched solid density functional theory (QSDFT) kernel, assuming a carbon material with cylindrical pores. All samples were degassed for 12 h at 80 °C to remove attached gases and water before each measurement. Time-of-flight secondary ion mass spectrometry (ToF-SIMS) studies were carried out on a *M6 Plus* instrument by *IONTOF GmbH* (Münster, Germany), in which a ToF-SIMS and an in situ scanning probe microscopy (SPM) module are combined. The instrument is equipped with a 30 keV bismuth liquid metal ion gun (LMIG, nanoprobe 50) for analysis, and a gas cluster ion beam (GCIB) for depth profiling. All measurements, which include surface imaging and depth profiling, were performed in negative polarity using Bi_3^+ primary ions with an energy of 30 keV. Moreover, the surfaces were flooded with low-energy electrons for all measurements to avoid surface charging. For surface imaging of the carbon thin films, the fast-imaging mode (unbunched mode, full width at half maximum (FWHM) of $m/\Delta m = 7390$ at $m/z = 48.00$ (C_4^-)) was used in combination with the delayed extraction analyzer setting, to allow 2D studies of the morphology and chemical environment of the thin film surfaces. The analysis area was 200 µm × 200 µm, and the plane was rasterized with (512 × 512) pixels. The primary ion current was ≈0.04 pA with a cycle time of 50 µs. Depth profiles were recorded in spectrometry mode (bunched mode, FWHM of $m/\Delta m = 14044$ at $m/z = 48.00$ (C_4^-)) providing a high signal intensity, and were combined with the high mass resolution setting of the analyzer, which enables simultaneously a high mass resolution. In order to record the 3D composition and the accessibility of the mesoporous thin films, Ar_{1000}-cluster (cluster distribution with a maximum at 1000 Ar atoms) with an energy of 10 keV were used for sputtering. For analysis, an area of 200 µm × 200 µm was placed in the sputter crater of 300 µm × 300 µm. The larger sputter crater was chosen to avoid crater wall effects on the extracted secondary ions. Every analysis plane of the depth profile was rasterized with (128 × 128) pixels, and between three sputters, six analysis frames were performed after waiting for 1 s in random raster mode. The primary ion current was ≈0.4–0.5 pA and the sputter current was 9.0 nA at a duty cycle of 100 µs. AFM line scans of the sputter crater were performed with the in situ SPM module of the *M6 Plus*. Line scans were recorded with a Ni cantilever with a pyramidal boron-doped diamond tip in intermittent contact mode. The whole data recording and analysis of the SIMS and SPM measurements were carried out with the *SurfaceLab 7.4* software (*IONTOF GmbH*). Prior to analysis of the pore accessibility, both carbon thin films were immersed by a 1 M tracing solution. For this purpose, 9 mg $LiBF_4$ (98%, Sigma Aldrich) were dissolved in 1 mL isopropanol upon stirring at room temperature for 5 min. One drop of the colorless tracing solution was dropped on every sample with the aid of a Pasteur pipette, and the films were dried under ambient conditions for 15 min. After careful removal of remaining droplets with a tissue, the samples were further dried in an oven at 80 °C for 5 h. Phase composition of the IrO_2 thin film was studied by grazing incidence X-ray diffraction (GIXRD) using an *XRDynamic 500* diffractometer by *Anton Paar* with an incidence angle of 2°. A 2θ range of 10 until 90° was covered with a step size of 0.01° and a scanning time of 100 s per step. The optics were composed of a Cu Kα ($\lambda = 1.5406$ Å) X-ray source, a divergence slit of 0.03°, a beam mask of 10 mm, and a primary and secondary solar slit of 0.05 rad each. The Raman spectrum was recorded with a *Senterra* spectroscope by *Bruker* equipped with a laser of 532 nm wavelength and a power of 20 mW. After co-addition of 30 scans of 10 s each in the spectral range of 80–4450 cm^{-1}, the data were exported with the corresponding *OPUS* software. The thickness and refractive index of the IrO_2 thin film were measured with a *SE400Adv* laser ellipsometer by *Sentech* equipped with a 633 nm HeNe laser. Angles of 55, 65, and 75° were used for the measurement, and a model consisting of an overlaying air layer ($n = 1.0000$), a 100 nm IrO_2 ($n = 2.5000$) deposition layer, and a silicon substrate ($n = 3.8714$) was assumed. X-ray reflectometry (XRR) of metal oxide thin films on silicon wafers was carried out on a *Rigaku SmartLab* diffractometer operated with a Cu Kα ($\lambda = 1.5406$ Å) X-ray generator (power of 9 kW and voltage of 45 kV). The optics of the parallel-beam geometry comprised a 0.05 mm incident slit, a Ge(220) monochromator, a 5 mm length-limiting slit, a 0.1 mm receiving slit, and a 2.5° Soller slit. The $2\theta/\omega$ scans were recorded with a scan speed of 0.4° min^{-1} and a step size of 0.01° in a 2θ range from 0 to 6° with a *HyPix3000(H)* detector. All XRR curves were fitted with the corresponding *SmartLab Studio II* software, assuming a model composed of a Si substrate (density of 2.329 g cm^{-3} and roughness of 0.5 nm), an SiO_2 interface (thickness of 2 nm according to ellipsometry), and an IrO_2 thin film. The electrochemical properties of the mesoporous thin films were investigated on both Ti and Si substrates at room temperature and on Si wafers between –50 and 50 °C (every 5 °C). In this regard, electrochemical impedance spectroscopy (EIS) perpendicular to the thin film surface was performed in a frequency range between 10^7 and 10 Hz with an *Alpha-A* impedance bridge from *Novocontrol Technologies GmbH & Co. KG* and an AC amplitude of 100 mV. In-plane electric transport measurements along the thin film surface were performed on silicon wafers in van-der-Pauw geometry. Platinum was used as electrical contacts, which was deposited at all four corners of the specimen using pulsed laser deposition (PLD). The deposition was conducted at room temperature under argon atmosphere ($p = 2$ Pa) with a *Coherent* KrF excimer laser ($\lambda = 248$ nm) using 10000 pulses with an energy of 400 mJ each and a repetition rate of 6 Hz. The PLD mask resulted in deposition of square-shaped platinum contacts (2 mm x 2 mm) in the thin film's corner with a distance of 0.5 mm to each edge. The transport measurements were conducted using a superconducting magnetic system from *Oxford*

Instruments equipped with a variable temperature insert. The temperature-dependent resistivity was measured in the temperature range between 10 and 280 K using a current varying between 10 nA and 10 mA depending on the resistivity of the sample. Hall measurements were performed at 280 K varying the magnetic field between −10 T and +10 T perpendicular to the samples' surface. The electrochemical stability of the carbon thin film was tested in a custom-made PEEK flow cell equipped with a glassy carbon counter electrode (3 mm carbon disk cladded with 3 mm PEEK, eDAQ) and an Ag/AgCl reference electrode (2 mm wide leakless miniature electrode filled with 3.4 M KCl, eDAQ). The carbon sample on polished titanium was contacted from the backside (i.e., the Ti metal substrate) with a stainless steel lid closing the flow cell. The 0.5 M sulfuric acid used as electrolyte (prepared with 486 mL of deionized water and 14 mL of a 95% sulfuric acid purchased from VWR Chemicals) was pumped through the cell using a *BT100-3J* peristaltic pump (*Longer*) equipped with a *DG-1-6* pump head with a flow rate of 2 mL min^{-1} (motor rotation of 10.6 rpm). Cyclic voltammetry (CV) was performed with an *Autolab PGSTAT302N* potentiostat by *Metrohm*, and all electrode potentials were corrected for the Ohmic (iR) drop and given vs. the standard hydrogen electrode (SHE) throughout this article. Conditioning of the carbon sample was executed by recording 50 CV cycles between 0.10 and 1.50 V and 40 cycles between 1.25 and 1.40 V against the reference electrode with a scan rate of 0.05 V s^{-1}. After equilibration of the open-circuit potential (OCP), the actual CV scans (0.01 V s^{-1}) were measured. X-ray photoelectron spectroscopy (XPS) measurements were conducted with a *PHI 5000 VersaProbe IV* Scanning ESCA Microprobe (*Physical Electronics*) using monochromatized Al Kα X-ray radiation ($h\nu$ = 1486.6 eV) in high power mode (with a beam diameter of 200 µm, an X-ray power of 50 W, and an X-ray lamp voltage of 15 kV). Carbon powders were filled in a Teflon sample cap and attached to the XPS sample holder with an isolating tape. Survey spectra were recorded with time steps of 50 ms, a step size of 0.2 eV, and an analyzer pass energy of 140 eV. The sample surface was charge-neutralized with slow electrons and argon ions, and the pressure was kept between 10^{-7} and 10^{-6} Pa during the measurement. All spectra were analyzed using the *CasaXPS* software.

Supporting Information

Supporting Information is available from the Wiley Online Library or from the author.

Acknowledgements

The authors thank Raoul Brand and Rafael Meinusch (both Justus Liebig University) for gas physisorption measurements, Sascha Prentzel and Helmut Schlaad (both University of Potsdam) for GPC experiments, and Mengnan Wang (Swansea University) for TEM measurements. Furthermore, Matteo Crisci is acknowledged for XPS measurements as well as Florian Rink for PLD sputtering and Limei Klar for recording Raman spectra of the carbon powders (all Justus Liebig University). L.W. thanks the Funds of the Chemical Industry (FCI) and C.G. the German Academic Scholarship Foundation for financial support each. B.S. and M.R. acknowledge funding by the German Research Foundation (DFG) within the project 390874152 (POLiS Cluster of Excellence). M.T.E. acknowledges financial support by the Heisenberg Program of the DFG (498993886, grant no. EL 863/6-1). M.R. thanks the Federal Ministry of Education and Research (BMBF) for funding of the SIMS-AFM machine within the ProGraL project (grant no. 03XP0427).

Open access funding enabled and organized by Projekt DEAL.

Conflict of Interest

The authors declare no conflict of interests.

Author Contributions

The manuscript was written through contributions of all authors. All authors have given approval to the final version of the manuscript.

Data Availability Statement

The raw data of this study are openly available in Zenodo: https://doi.org/10.5281/zenodo.17591320.

Keywords

amorphous-to-crystalline transition, block copolymers, electric transport, electrocatalysis, hard carbons, mesoporous carbon, secondary ion mass spectrometry, soft templating

Received: August 11, 2025
Revised: September 25, 2025
Published online: October 21, 2025

[1] J. Kibsgaard, I. Chorkendorff, *Nat. Energy* **2019**, *4*, 430.
[2] M. Carmo, D. L. Fritz, J. Mergel, D. Stolten, *Int. J. Hydrogen Energy* **2013**, *38*, 4901.
[3] Y. Deng, Y. Cai, Z. Sun, D. Gu, J. Wei, W. Li, X. Guo, J. Yang, D. Zhao, *Adv. Funct. Mater.* **2010**, *20*, 3658.
[4] M. R. Benzigar, S. N. Talapaneni, S. Joseph, K. Ramadass, G. Singh, J. Scaranto, U. Ravon, K. Al-Bahily, A. Vinu, *Chem. Soc. Rev.* **2018**, *47*, 2680.
[5] X. Wang, C. Liang, S. Dai, *Langmuir* **2008**, *24*, 7500.
[6] D. Gang, Z. Uddin Ahmad, Q. Lian, L. Yao, M. E. Zappi, *Chem. Eng. J.* **2021**, *403*, 126286.
[7] D. Bernsmeier, L. Chuenchom, B. Paul, S. Rümmler, B. Smarsly, R. Kraehnert, *ACS Catal.* **2016**, *6*, 8255.
[8] H. Nishihara, T. Kyotani, *Adv. Mater.* **2012**, *24*, 4473.
[9] S. Tanaka, N. Nishiyama, Y. Egashira, K. Ueyama, *Chem. Commun.* **2005**, 2125.
[10] Y. Zhang, Z. Qiang, B. D. Vogt, *RSC Adv.* **2014**, *4*, 44858.
[11] S. Kataoka, T. Yamamoto, Y. Inagi, A. Endo, M. Nakaiwa, T. Ohmori, *Carbon* **2008**, *46*, 1358.
[12] B. D. Vogt, V. L. Chavez, M. Dai, M. R. C. Arreola, L. Song, D. Feng, D. Zhao, G. M. Perera, G. E. Stein, *Langmuir* **2011**, *27*, 5607.
[13] A. Labiano, M. Dai, W.-S. Young, G. E. Stein, K. A. Cavicchi, T. H. Epps, B. D. Vogt, *J. Phys. Chem. C* **2012**, *116*, 6038.
[14] J. Xue, G. Singh, Z. Qiang, A. Karim, B. D. Vogt, *Nanoscale* **2013**, *5*, 7928.
[15] T. Kimura, A. M. Emre, K. Kato, Y. Hayashi, *J. Mater. Chem. A* **2013**, *1*, 15135.
[16] Z. Qiang, Y. Guo, H. Liu, S. Z. D. Cheng, M. Cakmak, K. A. Cavicchi, B. D. Vogt, *ACS Appl. Mater. Interfaces* **2015**, *7*, 4306.
[17] D. Bernsmeier, M. Bernicke, E. Ortel, R. Schmack, J. Polte, R. Kraehnert, *J. Catal.* **2017**, *355*, 110.
[18] D. Bernsmeier, R. Sachse, M. Bernicke, R. Schmack, F. Kettemann, J. Polte, R. Kraehnert, *J. Catal.* **2019**, *369*, 181.
[19] R. Sachse, D. Bernsmeier, R. Schmack, I. Häusler, A. Hertwig, K. Kraffert, J. Nissen, R. Kraehnert, *Catal. Sci. Technol.* **2020**, *10*, 2057.
[20] J. Schuster, R. Köhn, A. Keilbach, M. Döblinger, H. Amenitsch, T. Bein, *Chem. Mater.* **2009**, *21*, 5754.
[21] Z. Qiang, J. Xue, G. E. Stein, K. A. Cavicchi, B. D. Vogt, *Langmuir* **2013**, *29*, 9950.
[22] Z. Qiang, Y. Zhang, Y. Wang, S. M. Bhaway, K. A. Cavicchi, B. D. Vogt, *Carbon* **2015**, *82*, 51.

[23] J. Jin, N. Nishiyama, Y. Egashira, K. Ueyama, *Chem. Commun* **2009**, 1371.
[24] D. Feng, Y. Lv, Z. Wu, Y. Dou, L. Han, Z. Sun, Y. Xia, G. Zheng, D. Zhao, *J. Am. Chem. Soc.* **2011**, *133*, 15148.
[25] S. Tanaka, A. Doi, N. Nakatani, Y. Katayama, Y. Miyake, *Carbon* **2009**, *47*, 2688.
[26] L. Song, D. Feng, N. J. Fredin, K. G. Yager, R. L. Jones, Q. Wu, D. Zhao, B. D. Vogt, *ACS Nano* **2010**, *4*, 189.
[27] T. Mitome, Y. Uchida, Y. Egashira, N. Nishiyama, *Colloids Surfaces A Physicochem. Eng. Asp.* **2014**, *449*, 51.
[28] S. Tanaka, Y. Katayama, M. P. Tate, H. W. Hillhouse, Y. Miyake, *J. Mater. Chem.* **2007**, *17*, 3639.
[29] D. Gebauer, A. Völkel, H. Cölfen, *Science* **2008**, *322*, 1819.
[30] D. Gebauer, H. Cölfen, *Nano Today* **2011**, *6*, 564.
[31] D. Gebauer, M. Kellermeier, J. D. Gale, L. Bergström, H. Cölfen, *Chem. Soc. Rev.* **2014**, *43*, 2348.
[32] J. J. De Yoreo, P. U. P. A. Gilbert, N. A. J. M. Sommerdijk, R. L. Penn, S. Whitelam, D. Joester, H. Zhang, J. D. Rimer, A. Navrotsky, J. F. Banfield, A. F. Wallace, F. M. Michel, F. C. Meldrum, H. Cölfen, P. M. Dove, *Science* **2015**, *349*, 498.
[33] A.-W. Xu, Y. Ma, H. Cölfen, *J. Mater. Chem.* **2007**, *17*, 415.
[34] A. Oberlin, *Carbon* **1984**, *22*, 521.
[35] F. Badaczewski, M. O. Loeh, T. Pfaff, S. Dobrotka, D. Wallacher, D. Clemens, J. Metz, B. M. Smarsly, *Carbon* **2019**, *141*, 169.
[36] R. Song, H. Cölfen, *Adv. Mater.* **2010**, *22*, 1301.
[37] M. Jehannin, A. Rao, H. Cölfen, *J. Am. Chem. Soc.* **2019**, *141*, 10120.
[38] M. Niederberger, H. Cölfen, *Phys. Chem. Chem. Phys.* **2006**, *8*, 3271. .
[39] T. Wang, A. Xu, H. Cölfen, *Angew. Chem., Int. Ed.* **2006**, *45*, 4451.
[40] L.-B. Mao, H.-L. Gao, H.-B. Yao, L. Liu, H. Cölfen, G. Liu, S.-M. Chen, S.-K. Li, Y.-X. Yan, Y.-Y. Liu, S.-H. Yu, *Science* **2016**, *354*, 107.
[41] F. C. Meldrum, H. Cölfen, *Chem. Rev.* **2008**, *108*, 4332.
[42] C. Liang, K. Hong, G. A. Guiochon, J. W. Mays, S. Dai, *Angew. Chem., Int. Ed.* **2004**, *43*, 5785.
[43] Y. Meng, D. Gu, F. Zhang, Y. Shi, H. Yang, Z. Li, C. Yu, B. Tu, D. Zhao, *Angew. Chem., Int. Ed.* **2005**, *44*, 7053.
[44] E. Axente, M. Sopronyi, C. Matei Ghimbeu, C. Nita, A. Airoudj, G. Schrodj, F. Sima, *Carbon* **2017**, *122*, 484.
[45] S. Herou, M. C. Ribadeneyra, R. Madhu, V. Araullo-Peters, A. Jensen, P. Schlee, M. Titirici, *Green Chem.* **2019**, *21*, 550.
[46] X. Sun, W. Huang, C. Yang, F. Qi, J. Chen, N. Zhao, X. OuYang, *ACS Appl. Energy Mater.* **2023**, *6*, 6826.
[47] N. T. Rodrigues, F. D. Alves, A. Reis, *Langmuir* **2024**, *40*, 11371.
[48] A. Liang, C. Liu, P. S. Branicio, *Langmuir* **2024**, *40*, 10868.
[49] Y. Deng, T. Yu, Y. Wan, Y. Shi, Y. Meng, D. Gu, L. Zhang, Y. Huang, C. Liu, X. Wu, D. Zhao, *J. Am. Chem. Soc.* **2007**, *129*, 1690.
[50] H. N. Lokupitiya, A. Jones, B. Reid, S. Guldin, M. Stefik, *Chem. Mater.* **2016**, *28*, 1653.
[51] L. Q. Wagner, E. Prates da Costa, C. Glatthaar, F. Breckwoldt, M. Zecca, P. Centomo, X. Huang, C. Kübel, H. Schlaad, M. Kriechbaum, H. Amenitsch, M. Thommes, B. M. Smarsly, *Chem. Mater.* **2023**, *35*, 9879.
[52] C. Glatthaar, M. Wang, L. Q. Wagner, F. Breckwoldt, Z. Guo, K. Zheng, M. Kriechbaum, H. Amenitsch, M.-M. Titirici, B. M. Smarsly, *Chem. Mater.* **2023**, *35*, 10416.
[53] H. Oh, Y. J. Lee, E. J. Kim, J. Park, H.-E. Kim, H. Lee, H. Lee, B. J. Kim, *Nanoscale* **2024**, *16*, 879.
[54] D. Bernsmeier, M. Bernicke, E. Ortel, A. Bergmann, A. Lippitz, J. Nissen, R. Schmack, P. Strasser, J. Polte, R. Kraehnert, *ChemElectroChem* **2017**, *4*, 221.
[55] J. Willsau, J. Heitbaum, *J. Electroanal. Chem.* **1984**, *161*, 93.
[56] S. J. Ashton, M. Arenz, *Electrochem. Commun.* **2011**, *13*, 1473.
[57] L. Eifert, Z. Jusys, R. Banerjee, R. J. Behm, R. Zeis, *ACS Appl. Energy Mater.* **2018**, *1*, 6714.
[58] L. Eifert, Z. Jusys, R. J. Behm, R. Zeis, *Carbon* **2020**, *158*, 580.
[59] M. Schilling, A. Ershov, R. Debastiani, K. Duan, K. Köble, S. Scherer, L. Lan, A. Rampf, T. Faragó, M. Zuber, A. Cecilia, S. Liu, C. Liu, T. Baumbach, J. Li, P. Sui, R. Zeis, *Energy Adv* **2024**, *3*, 997.
[60] Y. Meng, D. Gu, F. Zhang, Y. Shi, L. Cheng, D. Feng, Z. Wu, Z. Chen, Y. Wan, A. Stein, D. Zhao, *Chem. Mater.* **2006**, *18*, 4447.
[61] L. Chuenchom, R. Kraehnert, B. M. Smarsly, *Soft Matter* **2012**, *8*, 10801.
[62] A. Šebenik, U. Osredkar, I. Vizovišek, *Polymer* **1981**, *22*, 804.
[63] Y. Lu, H. Fan, A. Stump, T. L. Ward, T. Rieker, C. J. Brinker, *Nature* **1999**, *398*, 223.
[64] C. J. Brinker, Y. Lu, A. Sellinger, H. Fan, *Adv. Funct. Mater.* **1999**, *11*, 579.
[65] D. Grosso, F. Cagnol, G. J. de, A. A. Soler-Illia, E. L. Crepaldi, H. Amenitsch, A. Brunet-Bruneau, A. Bourgeois, C. Sanchez, *Adv. Funct. Mater.* **2004**, *14*, 309.
[66] M. A. Soto-Oviedo, R. S. Lehrle, I. W. Parsons, M. A. De Paoli, *Polym. Degrad. Stab.* **2003**, *81*, 463.
[67] D. B. Schuepfer, F. Badaczewski, J. M. Guerra-Castro, D. M. Hofmann, C. Heiliger, B. Smarsly, P. J. Klar, *Carbon* **2020**, *161*, 359.
[68] A. C. Ferrari, D. M. Basko, *Nat. Nanotechnol.* **2013**, *8*, 235.
[69] A. Sadezky, H. Muckenhuber, H. Grothe, R. Niessner, U. Pöschl, *Carbon* **2005**, *43*, 1731.
[70] A. Kaniyoor, S. Ramaprabhu, *AIP Adv.* **2012**, *2*, 032183.
[71] R. Vidano, D. B. Fischbach, *J. Am. Ceram. Soc.* **1978**, *61*, 13.
[72] O. Osswald, M. O. Loeh, F. M. Badaczewski, T. Pfaff, H. E. Fischer, A. Franz, J. Hoffmann, M. Reehuis, P. J. Klar, B. M. Smarsly, *C* **2023**, *9*, 27.
[73] K. Faber, F. Badaczewski, W. Ruland, B. M. Smarsly, *Zeitschrift für Anorg. und Allg. Chemie* **2014**, *640*, 3107.
[74] W. Ruland, B. Smarsly, *J. Appl. Crystallogr.* **2002**, *35*, 624.
[75] O. Osswald, B. M. Smarsly, *C* **2022**, *8*, 78.
[76] J. W. Eaton, D. Bateman, S. Hauberg, R. Wehbring, **2023**.
[77] R. E. Franklin, *Proc. R. Soc. London. Ser. A* **1951**, *209*, 196.
[78] D. A. Stevens, J. R. Dahn, *J. Electrochem. Soc.* **2000**, *147*, 1271.
[79] Y. Youn, B. Gao, A. Kamiyama, K. Kubota, S. Komaba, Y. Tateyama, *npj Comput. Mater.* **2021**, *7*, 48.
[80] M. Thommes, C. Schlumberger, *Annu. Rev. Chem. Biomol. Eng.* **2021**, *12*, 137.
[81] K. Frisk, *Calphad* **2003**, *27*, 367.
[82] D. A. Andersson, P. A. Korzhavyi, B. Johansson, *Calphad* **2008**, *32*, 543.
[83] S. Saha, B. M. Rajbongshi, V. Ramani, A. Verma, *Int. J. Hydrogen Energy* **2021**, *46*, 12801.
[84] W. Yan, Y. Zhang, L. Chen, J. Luo, P. Pang, X. Zhang, B. Liao, M. Ying, *Diam. Relat. Mater.* **2021**, *120*, 108628.
[85] S.-Y. Lin, X. Zhang, *J. Power Sources* **2015**, *294*, 354.
[86] T. Weber, J. Pfrommer, M. J. S. Abb, B. Herd, O. Khalid, M. Rohnke, P. H. Lakner, J. Evertsson, S. Volkov, F. Bertram, R. Znaiguia, F. Carla, V. Vonk, E. Lundgren, A. Stierle, H. Over, *ACS Catal.* **2019**, *9*, 6530.
[87] R. Sachse, M. Pflüger, J.-J. Velasco-Vélez, M. Sahre, J. Radnik, M. Bernicke, D. Bernsmeier, V.-D. Hodoroaba, M. Krumrey, P. Strasser, R. Kraehnert, A. Hertwig, *ACS Catal.* **2020**, *10*, 14210.
[88] H. Over, *ACS Catal.* **2021**, *11*, 8848.
[89] D. D. Matienzo, D. Settipani, E. Instuli, T. Kallio, *Catalysts* **2020**, *10*, 92.
[90] W. Li, J. Lv, D. Liu, W. Cai, X. Chen, Q. Huang, L. Wang, B. Wang, *Chem. Mater.* **2023**, *35*, 3892.
[91] D. Bernsmeier, M. Bernicke, R. Schmack, R. Sachse, B. Paul, A. Bergmann, P. Strasser, E. Ortel, R. Kraehnert, *ChemSusChem* **2018**, *11*, 2367.
[92] M. Bernicke, E. Ortel, T. Reier, A. Bergmann, J. Ferreira De Araujo, P. Strasser, R. Kraehnert, *ChemSusChem* **2015**, *8*, 1908.

[93] Y. S. Huang, S. S. Lin, C. R. Huang, M. C. Lee, T. E. Dann, F. Z. Chien, *Solid State Commun.* **1989**, *70*, 517.
[94] A. Baptiste, A. Gibaud, J. F. Bardeau, K. Wen, R. Maoz, J. Sagiv, B. M. Ocko, *Langmuir* **2002**, *18*, 3916.
[95] A. Gibaud, S. Hazra, *Curr. Sci.* **2000**, *78*, 1467.
[96] S. Dourdain, J. F. Bardeau, M. Colas, B. Smarsly, A. Mehdi, B. M. Ocko, A. Gibaud, *Appl. Phys. Lett.* **2005**, *86*, 113108.
[97] S. Dourdain, A. Mehdi, J. F. Bardeau, A. Gibaud, *Thin Solid Films* **2006**, *495*, 205.
[98] Y. Minhao, M. J. Henderson, A. Gibaud, *Thin Solid Films* **2009**, *517*, 3028.
[99] A. Gibaud, S. Dourdain, G. Vignaud, *Appl. Surf. Sci.* **2006**, *253*, 3.
[100] Y. P. Feng, S. K. Sinha, E. E. Fullerton, G. Grübel, D. Abernathy, D. P. Siddons, J. B. Hastings, *Appl. Phys. Lett.* **1995**, *67*, 3647.
[101] A. K. Goel, G. Skorinko, F. H. Pollak, *Phys. Rev. B* **1981**, *24*, 7342.
[102] C. Boissiere, D. Grosso, S. Lepoutre, L. Nicole, A. B. Bruneau, C. Sanchez, *Langmuir* **2005**, *21*, 12362.
[103] P. Cop, K. Hess, S. Werner, R. Meinusch, B. M. Smarsly, H. Kozuka, *Langmuir* **2019**, *35*, 16427.
[104] D. A. Doshi, A. Gibaud, V. Goletto, M. Lu, H. Gerung, B. Ocko, S. M. Han, C. J. Brinker, *J. Am. Chem. Soc.* **2003**, *125*, 11646.
[105] J. K. Eckhardt, C. Heiliger, M. T. Elm, *ACS Appl. Mater. Interfaces* **2023**, *15*, 35332.
[106] M. Einert, C. Wessel, F. Badaczewski, T. Leichtweiß, C. Eufinger, J. Janek, J. Yuan, M. Antonietti, B. M. Smarsly, *Macromol. Chem. Phys.* **2015**, *216*, 1930.
[107] A. Kanapitsas, C. Tsonos, D. Triantis, I. Stavrakas, C. Anastasiadis, P. Photopoulos, P. Pissis, V. Em Vamvakas, *Thin Solid Films* **2010**, *518*, 2357.
[108] C. Michel, S. D. Baranovskii, P. J. Klar, P. Thomas, B. Goldlücke, *Appl. Phys. Lett.* **2006**, *89*, 2.
[109] T. F. Rosenbaum, R. F. Milligan, M. A. Paalanen, G. A. Thomas, R. N. Bhatt, W. Lin, *Phys. Rev. B* **1983**, *27*, 7509.
[110] I. B. Olenych, L. S. Monastyrskii, O. I. Aksimentyeva, Y. I. Eliyashevskyy, I. S. Girnyk, M. S. Rudko, *Mol. Cryst. Liq. Cryst.* **2020**, *700*, 88.
[111] C. Jagannath, Z. W. Grabowski, A. K. Ramdas, *Phys. Rev. B* **1981**, *23*, 2082.
[112] M. T. Elm, P. Uredat, J. Binder, L. Ostheim, M. Schäfer, P. Hille, J. Müßener, J. Schörmann, M. Eickhoff, P. J. Klar, *Nano Lett.* **2015**, *15*, 7822.
[113] W. R. Thurber, R. L. Mattis, Y. M. Liu, J. J. Filliben, *J. Electrochem. Soc.* **1980**, *127*, 1807.
[114] S. Duran, A. Grimaud, M. Faustini, J. Peron, *Chem. Mater.* **2023**, *35*, 8590.
[115] H. Liu, Q. Xu, C. Yan, *Electrochem. Commun.* **2013**, *28*, 58.
[116] M. D. Hawley, S. W. Feldberg, *J. Phys. Chem.* **1966**, *70*, 3459.
[117] L. Zeng, B. Yuan, Q. Zhou, *Langmuir* **2024**, *40*, 24696.
[118] T. Shen, X. Chen, Z. Hu, Z. Yan, L. Yang, H. Sun, R. Zhang, H.-Y. Yu, *Langmuir* **2025**, *41*, 694.
[119] P. Hartmann, D. K. Lee, B. M. Smarsly, J. Janek, *ACS Nano* **2010**, *4*, 3147.
[120] M. Kopeć, R. Yuan, E. Gottlieb, C. M. R. Abreu, Y. Song, Z. Wang, J. F. J. Coelho, K. Matyjaszewski, T. Kowalewski, *Macromolecules* **2017**, *50*, 2759.
[121] M. Fantin, A. A. Isse, A. Venzo, A. Gennaro, K. Matyjaszewski, *J. Am. Chem. Soc.* **2016**, *138*, 7216.